

Microscopic origin of the chiroptical response of optical media

Matthew S. Davis^{1, 2, 3*}, Wenqi Zhu^{1, 2}, Jay K. Lee³, Henri J. Lezec¹ and Amit Agrawal^{1, 2*}

¹Center for Nanoscale Science and Technology, National Institute of Standards and Technology, Gaithersburg, MD 20899 USA

²Maryland NanoCenter, University of Maryland, College Park, MD 20742 USA

³Department of Electrical Engineering and Computer Science, Syracuse University, Syracuse, NY 13244 USA

*Corresponding authors: Email: matthew.davis@nist.gov; amit.agrawal@nist.gov

One Sentence Summary: A generalized model framework for the design and study of chiroptical systems.

The potential for enhancing the optical activity of natural chiral media using engineered nanophotonic components has been central in the quest towards developing next-generation circular-dichroism spectroscopic techniques. Through confinement and manipulation of optical fields at the nanoscale, ultrathin flat optical elements composed of an array of metallic or dielectric nanostructures have enabled a path towards achieving orders of magnitude enhancements in the chiroptical response. Here, we develop a model framework to describe the underlying physics governing the origin of chiroptical response in optical media. The model identifies optical activity to fundamentally originate from electromagnetic coupling to the hybridized eigen-states of a coupled electron-oscillator system, whereas differential near-field absorption of opposite handedness light, though resulting in a far-field chiroptical response, is shown to have incorrectly been identified as optical activity. We validate the model predictions using experimental measurements, and show it to also be consistent with observations in the literature. The work provides a generalized framework for the design and study of chiroptical systems.

Introduction

Chirality is the geometric property of an object being non-superimposable on its mirror image along any symmetry axis, and is ubiquitous in the natural world. For example, sugars, proteins, and deoxyribonucleic acids are chiral molecules essential to the functioning and continuation of biological processes. The two variants of a chiral molecule, known as enantiomers, are chemically identical but structured in either a left or a right-handed arrangement. Biological systems on Earth have evolved to prefer left-handed enantiomers – a property referred to as homochirality (1). A comprehensive understanding of the evolutionary mechanisms responsible for homochirality remains elusive, but investigations are yielding insights into the origins of life on Earth (2) and even in the search for extraterrestrial life (3). Many biochemical processes, to function correctly, also require a particular handedness enantiomer. This is observed in the metabolism of pharmaceuticals such as thalidomide (4) and penicillamine (5) wherein one enantiomer produces medicinal effects and the other toxicity. Thus, enantiomer discrimination techniques such as circular dichroism (CD) spectroscopy are essential for minimizing the toxic effects of medications (6, 7), developing effective treatments for diseases (8, 9), and probing the nature of chiral systems (10). In addition to enantiomer discrimination, CD spectroscopy also provides information on protein secondary structures crucial to understanding protein folding (11, 12). This understanding benefits the development of treatments for several deadly diseases such as Alzheimer's, Parkinson's, and some cancers (13). However, the inherently weak CD response from natural molecular systems coupled with the limited sensitivity of conventional CD spectroscopic techniques have placed an upper-limit on the overall detection sensitivity. In recent years, engineered ultrathin nanoscale optical devices, composed of an array of metallic or dielectric nanostructures, have been used to enhance the CD response of natural chiral media by several orders in magnitude, suggesting the possibility of next-generation CD spectroscopic techniques with significantly improved measurement sensitivities (14, 15). However, the underlying phenomena governing the microscopic origin of the chiroptical response from nano-optical devices is still not well understood. Here, we present, and experimentally validate, a generalized model that identifies the fundamental origin

of optical activity in a chiral medium, and unifies the distinct chiroptical phenomenon observed in literature under a single theoretical framework.

Circular dichroism is a measure of the optical activity in a chiroptical medium, and is characterized by the differential absorption between right and left circularly polarized light (RCP and LCP, respectively). Since chiral media exhibits circular birefringence, optical activity can also be characterized by the degree of rotation of a linearly polarized light as it propagates through it – a phenomenon commonly referred to as optical rotary dispersion (ORD). CD and ORD are both synonymous with optical activity since they originate from the same quantum mechanical phenomenon, and are related to each other through the Kramers-Kronig transformation (16). We define a generalized far-field chiroptical (CO) response of an optical medium as the differential transmission (or reflection) response to RCP and LCP source fields, quantitatively expressed for transmission measurements as $CO(\omega) = T_{RCP}(\omega) - T_{LCP}(\omega)$, where T_{RCP} (T_{LCP}) is the spectral intensity transmission for illumination with a RCP (LCP) light. As we demonstrate in this paper, a far-field CO response does not always correspond to CD, and can originate from other microscopic phenomenon not related to optical activity. Hence, careful consideration must be given to the interpretation of CO measurements (17-19).

We identify three primary CO response types that are experimentally characterized and theoretically studied within the framework of an all-purpose, generalized coupled-oscillator model described in the next section. We demonstrate optical activity to fundamentally originate from the accessibility of RCP and LCP light to the hybridized energy-shifted eigen states of a coupled electron-oscillator system – a result that is consistent with the predictions of the Born-Kuhn model (20). Subtracting the two energy-shifted spectral responses from one another, upon illumination with RCP and LCP light respectively, results in a far-field CO response associated with optical activity, which we hereafter refer to as CO_{OA} . Differential absorption to opposite handedness light, not related to optical activity, but originating from near-field absorption modes in planar chiral media has also been shown to produce a far-field CO response, which we refer to as CO_{abs} (21, 22). In contrast to CO_{OA} , CO_{abs} results from a difference in amplitudes between the transmission

(or reflection) spectra without any associated spectral shift when subjected to illumination with opposite handedness light (23). Finally, by employing birefringence in an all-dielectric metamaterial acting as a uniaxial or a biaxial medium, a strong far-field CO response has been observed through spatial filtering of either the RCP or the LCP light (19, 24, 25). This response type, referred to here as CO_{axial} , is also not associated with optical activity in the underlying optical medium. Since the three response types can be present in a single CO measurement, we express the total chiroptical response of optical media as $CO = CO_{\text{OA}} + CO_{\text{abs}} + CO_{\text{axial}}$ where $CO_{\text{OA}} \neq CO_{\text{abs}} \neq CO_{\text{axial}}$. Note that these phenomena have been separately observed experimentally (20-27), and the former two are analytically described in previous works (20, 22, 28) – however, independent models have been used to describe them without any clear relation between them. No analytical model has yet successfully described the various types of CO responses observed in literature under a single comprehensive theoretical framework. The model developed here provides an analytical foundation for a generalized CO response from an optical medium, and suggests easy-to-implement methods for identifying the presence of, and distinguishing between, the distinct phenomena present in a CO measurement that may or may not originate from optical activity. The model predictions are experimentally validated using far-field CO measurements on engineered nanoscale plasmonic devices at optical frequencies, and are shown to also be consistent with observations in the literature.

Results

The Generalized Coupled Oscillator Model

We model the microscopic chiroptical response of optical media at the molecular unit-cell level using two lossy coupled electron oscillators. The two oscillators are assumed to be arbitrarily located and oriented relative to each other, and interacting with an arbitrarily polarized light at oblique incidence with electric field $\vec{E}_0 e^{i(\vec{k} \cdot \vec{r} - \omega t)}$ (Figure 1A), where \vec{k} and ω are the wavevector and frequency of the incident light, respectively. These coupled oscillators constitute a single molecular unit-cell described by a pair of fully vectorial second-order coupled differential equations:

$$\partial_t^2 \bar{u}_1 + \gamma_1 \partial_t \bar{u}_1 + \omega_1^2 \bar{u}_1 + \zeta_{2,1} u_2 \hat{u}_1 = -\frac{e}{m^*} (\vec{E}_0 \cdot \hat{u}_1) \hat{u}_1 e^{i(\vec{k} \cdot \vec{r}_1 - \omega t)} \quad (1.1)$$

$$\partial_t^2 \bar{u}_2 + \gamma_2 \partial_t \bar{u}_2 + \omega_2^2 \bar{u}_2 + \zeta_{1,2} u_1 \hat{u}_2 = -\frac{e}{m^*} (\vec{E}_0 \cdot \hat{u}_2) \hat{u}_2 e^{i(\vec{k} \cdot \vec{r}_2 - \omega t)} \quad (1.2)$$

Each oscillator \bar{u}_i is characterized by an oscillation amplitude $u_i(\omega, t)$, resonant frequency ω_i , damping factor γ_i , and cross-coupling strength $\zeta_{i,j}(\omega)$, representing the electromagnetic interaction between the oscillators, for $i, j = 1, 2$. The oscillator locations are given by $\vec{r}_i = \vec{r}_0 + \delta\vec{r}_i$, with $\delta\vec{r}_i$ being the oscillator displacement from the molecular center of mass \vec{r}_0 (Figures 1B-D). Furthermore, the electron-oscillators are described by a charge e and an effective mass m^* .

Inserting the time harmonic expressions $\bar{u}_1(\omega, t) = \hat{u}_1 u_1 e^{-i\omega t}$ and $\bar{u}_2(\omega, t) = \hat{u}_2 u_2 e^{-i\omega t}$ into equations (1.1-1.2) and using the substitution $\Omega_k = \sqrt{\omega_k^2 - \omega^2 - i\gamma_k \omega}$ for $k = 1, 2$ gives closed form solutions for the two oscillation amplitudes expressed as (Supplementary Section S1):

$$u_1(\omega) = \frac{-e}{m^*} \left[\frac{\Omega_2^2 (\vec{E}_0 \cdot \hat{u}_1) e^{i\vec{k} \cdot \delta\vec{r}_1} - \zeta_{2,1} (\vec{E}_0 \cdot \hat{u}_2) e^{i\vec{k} \cdot \delta\vec{r}_2}}{\Omega_1^2 \Omega_2^2 - \zeta_{1,2} \zeta_{2,1}} \right] e^{i\vec{k} \cdot \vec{r}_0} \quad (2.1)$$

$$u_2(\omega) = \frac{-e}{m^*} \left[\frac{\Omega_1^2 (\vec{E}_0 \cdot \hat{u}_2) e^{i\vec{k} \cdot \delta\vec{r}_2} - \zeta_{1,2} (\vec{E}_0 \cdot \hat{u}_1) e^{i\vec{k} \cdot \delta\vec{r}_1}}{\Omega_1^2 \Omega_2^2 - \zeta_{1,2} \zeta_{2,1}} \right] e^{i\vec{k} \cdot \vec{r}_0} \quad (2.2)$$

Using equations (2.1) and (2.2), the medium's current density response $\vec{J}(\omega, t)$ to the driving source field can be calculated as (Supplementary Section S2):

$$\vec{J}(\omega, t) = \frac{-i\epsilon_0 \omega \omega_p^2}{\Omega_1^2 \Omega_2^2 - \zeta_{1,2} \zeta_{2,1}} \left\{ \left[\Omega_2^2 (\vec{E}_0 \cdot \hat{u}_1) - \zeta_{2,1} (\vec{E}_0 \cdot \hat{u}_2) e^{-i\vec{k} \cdot (\delta\vec{r}_1 - \delta\vec{r}_2)} \right] \hat{u}_1 + \left[\Omega_1^2 (\vec{E}_0 \cdot \hat{u}_2) - \zeta_{1,2} (\vec{E}_0 \cdot \hat{u}_1) e^{i\vec{k} \cdot (\delta\vec{r}_1 - \delta\vec{r}_2)} \right] \hat{u}_2 \right\} e^{i(\vec{k} \cdot \vec{r} - \omega t)} \quad (3)$$

where $\omega_p = \sqrt{ne^2/m^* \epsilon_0}$ is the plasma frequency, ϵ_0 is the permittivity of free-space, and n is the molecular unit-cell density. By rearranging equation (3), the current density response can be simplified as $\vec{J}(\omega, t) = -i\omega \epsilon_0 \chi \vec{E}_0 e^{i(\vec{k} \cdot \vec{r} - \omega t)}$ showing \vec{J} to be proportional to the product of the incident source field with a susceptibility tensor χ containing elements $\chi_{i,j}$ with $i, j = x, y, z$. The susceptibility tensor can be expressed in terms of a modified-dielectric tensor $\epsilon(k, \omega)$ and a non-locality tensor $\Gamma(k, \omega)$ as $\chi(k, \omega) =$

$\epsilon(k, \omega) + ik\Gamma(k, \omega)$, where the modified-dielectric tensor is related to the dielectric tensor as $\epsilon(k, \omega) = \epsilon(k, \omega) - \mathbf{I}$ (29). The non-locality tensor has previously been identified as related to the optical activity by the relations $\text{ORD} = \omega \text{Re}\{\Gamma\}/2c$ and $\text{CD} = 2\omega \text{Im}\{\Gamma\}/c$, where c is the speed of light in free-space (20). Full expressions for $\chi(k, \omega)$ along with derivations of expressions for $\epsilon(k, \omega)$ and $\Gamma(k, \omega)$ are given in Supplementary Section S3.

Since the relationship between the far-field and near-field CO response is typically approximated as $T_{RCP} - T_{LCP} \propto |\tilde{J}^{RCP}|^2 - |\tilde{J}^{LCP}|^2$, we express the CO response calculated using the model as $\text{CO} = |\tilde{J}^{RCP}|^2 - |\tilde{J}^{LCP}|^2$, where \tilde{J}^{RCP} and \tilde{J}^{LCP} indicate the current density response of the optical medium to RCP and LCP light, respectively. Expanding this term results in a concise expression for CO given as (Supplementary Section S4):

$$\text{CO}/\epsilon_0^2 \omega^2 = (\vec{\chi}_n \times \vec{\chi}_n^*) \cdot (\vec{E}_0 \times \vec{E}_0^*) \quad (4)$$

Equation (4) is expressed using the Einstein summation notation summed over $n = x, y, z$ where each susceptibility vector $\vec{\chi}_n$ contains elements $\chi_{n,k}$ for $k = x, y, z$ and is related to the dielectric and non-locality vectors by $\vec{\chi}_n = \vec{\epsilon}_n + ik\vec{\Gamma}_n$ (29). Note that the expression for CO is non-zero only if both (i) the incident source field is elliptically or circularly polarized, and (ii) the susceptibility terms are complex which occurs in the presence of either damping in the optical medium, γ_1 or $\gamma_2 \neq 0$, or spatial separation between the oscillators along the direction of source propagation, $\vec{k} \cdot (\delta\vec{r}_1 - \delta\vec{r}_2) \neq 0$ (Supplementary Section S3). Setting the two oscillators' orientation parallel to the x - y plane ($\theta_1 = \theta_2 = \pi/2$) and inserting this into equation (4) gives $\text{CO} = \epsilon_0^2 \omega^2 [(\vec{\epsilon}_n \times \vec{\epsilon}_n^*) + ik(\vec{\Gamma}_n \times \vec{\epsilon}_n^* - \vec{\epsilon}_n \times \vec{\Gamma}_n^*)] \cdot (\vec{E}_0 \times \vec{E}_0^*)$. This expression can be rewritten as the sum of two components, $\text{CO} = \Delta A = \Delta A_{\epsilon, \epsilon} + \Delta A_{\Gamma, \epsilon}$, where:

$$\Delta A_{\epsilon, \epsilon}/\epsilon_0^2 \omega^2 = (\vec{\epsilon}_n \times \vec{\epsilon}_n^*) \cdot (\vec{E}_0 \times \vec{E}_0^*) \quad (5.1)$$

$$\Delta A_{\Gamma, \epsilon}/\epsilon_0^2 \omega^2 = 2ik \text{Re}\{\vec{\Gamma}_n \times \vec{\epsilon}_n^*\} \cdot (\vec{E}_0 \times \vec{E}_0^*) \quad (5.2)$$

Here, $\Delta A_{\epsilon, \epsilon}$ is determined by the source interaction with the dielectric tensor, and $\Delta A_{\Gamma, \epsilon}$, by the source interaction with both the non-locality and dielectric tensors. In the limit where the spatial separation

between the oscillators is much smaller than the wavelength, $\vec{k} \cdot (\delta\vec{r}_1 - \delta\vec{r}_2) \ll 1$, equations (S12.1-S12.9) and (S13.1-S13.9) show that the dielectric tensor $\epsilon(k, \omega)$ only depends on ω whereas the non-locality tensor $\Gamma(k, \omega)$ becomes directly proportional to \hat{k} . This suggests an interesting dichotomy: the response $\Delta A_{\epsilon, \epsilon}$ is largely influenced by the source frequency corresponding to a temporal dispersion in the system, whereas $\Delta A_{\Gamma, \epsilon}$ is influenced by the direction of the incident field corresponding to a spatial dispersion in the system. Consistent with this, we show the dependence of $\Delta A_{\epsilon, \epsilon}$ on the angular separation between the oscillators in the direction of source electric-field rotation, and of $\Delta A_{\Gamma, \epsilon}$ on the separation between oscillators in the direction of the source propagation.

By further simplification, equations (5.1-5.2) can be rewritten as (Supplementary Section S4):

$$\Delta A_{\epsilon, \epsilon} = 2\epsilon_0^2 \omega^2 |E_0|^2 \cos \theta_0 \text{Im}\{\epsilon_{xx}^* \epsilon_{xy} + \epsilon_{yx}^* \epsilon_{yy}\} \quad (6.1)$$

$$\Delta A_{\Gamma, \epsilon} = 2\epsilon_0^2 \omega^2 |E_0|^2 \cos \theta_0 \text{Re}\{k[(\epsilon_{xy} \Gamma_{xx}^* - \epsilon_{xx} \Gamma_{xy}^*) + (\epsilon_{yy} \Gamma_{yx}^* - \epsilon_{yx} \Gamma_{yy}^*)]\} \quad (6.2)$$

Note that, in the absence of damping, $\epsilon_{i,j} = \epsilon_{i,j}^*$ for $i, j = x, y$, equation (6.1) reduces to $\Delta A_{\epsilon, \epsilon} = 0$. Furthermore, for an isotropic medium the diagonal elements of the dielectric tensor are equal and the oscillator coupling is symmetric ($\zeta_{1,2}(\omega) = \zeta_{2,1}(\omega)$) resulting in $\epsilon_{xx} = \epsilon_{yy}$ and $\epsilon_{xy} = \epsilon_{yx}$, respectively. Substituting these in equation (6.1), results in $\text{Im}\{\epsilon_{xx}^* \epsilon_{xy} + \epsilon_{yx}^* \epsilon_{yy}\} = 0$, or equivalently $\Delta A_{\epsilon, \epsilon} = 0$. Therefore, both damping and anisotropy in an optical medium are necessary to achieve a $\Delta A_{\epsilon, \epsilon}$ type chiroptical response. This conclusion is consistent with previous observation that absorption plays a critical role in generating a CO response (22, 23). Moreover, a CO response of the $\Delta A_{\epsilon, \epsilon}$ type has also been observed in lossy two-dimensional anisotropic plasmonic media (21, 30). We associate $\Delta A_{\epsilon, \epsilon}$ to the absorption based chiroptical response described earlier, CO_{abs} , noting again that this type of response is not related to optical activity. For the second response type, $\Delta A_{\Gamma, \epsilon}$, of equation (6.2) to be non-zero – a finite coupling between the oscillators is required, $\zeta_{1,2}(\omega) \neq 0$ and $\zeta_{2,1}(\omega) \neq 0$. Note that even for an isotropic medium with non-zero symmetric coupling ($\zeta_{1,2}(\omega) = \zeta_{2,1}(\omega)$), non-locality constants become $\Gamma_{xx} = \Gamma_{yy} = 0$ and $\Gamma_{xy} = -\Gamma_{yx}$ (Supplementary Section S3) resulting in a non-zero $\Delta A_{\Gamma, \epsilon}$ response. Hence

coupling between oscillators is a necessary condition to achieve $\Delta A_{\Gamma,\epsilon}$ type chiroptical response – a conclusion that is consistent with both the predictions of the Born-Kuhn model (20, 29), and with the treatment of bi-isotropic chiral media presented in ref. 31. We associate $\Delta A_{\Gamma,\epsilon}$ to the CO_{OA} type response described earlier which is fundamentally related to optical activity.

Further insights into the $\Delta A_{\epsilon,\epsilon}$ and $\Delta A_{\Gamma,\epsilon}$ response types can be achieved by expressing them in terms of the fundamental oscillator parameters of equations (1.1-1.2). By inserting expressions for the dielectric (equations S12.1-S12.9) and non-locality (equations S13.1-S13.9) constants into equations (6.1-6.2), and assuming $\phi_1 = 90^\circ$ for simplicity, $\Delta A_{\epsilon,\epsilon}$ and $\Delta A_{\Gamma,\epsilon}$ can be expressed as:

$$\Delta A_{\epsilon,\epsilon} = \kappa \omega \{ [\gamma_2(\omega^2 - \omega_1^2) - \gamma_1(\omega^2 - \omega_2^2)] \sin \phi_2 + (\gamma_2 \zeta_{1,2} - \gamma_1 \zeta_{2,1}) \cos[\vec{k} \cdot (\delta \vec{r}_1 - \delta \vec{r}_2)] \} \cos \phi_2 \quad (7.1)$$

$$\Delta A_{\Gamma,\epsilon} = \kappa \{ [\zeta_{2,1}(\omega^2 - \omega_1^2) + \zeta_{1,2}(\omega^2 - \omega_2^2)] \sin[\vec{k} \cdot (\delta \vec{r}_1 - \delta \vec{r}_2)] + \zeta_{1,2} \zeta_{2,1} \sin[2\vec{k} \cdot (\delta \vec{r}_1 - \delta \vec{r}_2)] \sin \phi_2 \} \cos \phi_2 \quad (7.2)$$

where the multiplication factor κ is defined as:

$$\kappa(\omega) = 2\epsilon_0^2 \omega^2 \omega_p^4 |E_0|^2 \cos \theta_0 / [(\omega_1^2 - \omega^2) - i\gamma_1 \omega][(\omega_2^2 - \omega^2) - i\gamma_2 \omega] - \zeta_{1,2} \zeta_{2,1}]^2.$$

By allowing the two oscillators to have the same damping coefficient, $\gamma_1 = \gamma_2 = \gamma$, and assuming the spatial separation between them to be much smaller than the wavelength, $\vec{k} \cdot (\delta \vec{r}_1 - \delta \vec{r}_2) \ll 1$, equations (7.1-7.2) reduce to:

$$\Delta A_{\epsilon,\epsilon} = \kappa \omega \gamma (\omega_2^2 - \omega_1^2) \sin \phi_2 \cos \phi_2 + \omega \gamma (\zeta_{1,2} - \zeta_{2,1}) \cos \phi_2 \quad (8.1)$$

$$\Delta A_{\Gamma,\epsilon} = \kappa \vec{k} \cdot (\delta \vec{r}_1 - \delta \vec{r}_2) [\zeta_{2,1}(\omega^2 - \omega_1^2) + \zeta_{1,2}(\omega^2 - \omega_2^2) + 2\zeta_{1,2} \zeta_{2,1} \sin \phi_2] \cos \phi_2 \quad (8.2)$$

We illustrate the behavior of these two CO response types in equations (8.1-8.2) by applying them to two Au nanocuboids, acting as oscillators, aligned parallel to the x - y plane (with $\phi_1 = 90^\circ$ and $\phi_2 = 45^\circ$) excited with a source field normally incident on the structure at angles, $\theta_0 = 0^\circ$ and $\theta_0 = 180^\circ$ (Figure 2A). We assume the two Au nanocuboids, separated along the direction of source propagation (z) by a distance $d_z = d_{1,z} - d_{2,z} = 200$ nm and located at $d_{1,y} = d_{2,x} = 100$ nm, to exhibit resonance at wavelengths $\lambda_1 = 750$ nm and $\lambda_2 = 735$ nm with $\zeta_{1,2}(\omega_1) = \zeta_{2,1}(\omega_2) = 1.6 \times 10^{29} \text{ s}^{-2}$. The following values for the

plasma frequency, $\omega_p = 1.37 \times 10^{16} \text{ s}^{-1}$, and damping coefficient, $\gamma = \gamma_1 = \gamma_2 = 1.22 \times 10^{14} \text{ s}^{-1}$, for Au in the near-infrared region are used (32). $\Delta A_{\epsilon,\epsilon}$ and $\Delta A_{\Gamma,\epsilon}$ plotted vs. incident wavelength λ_0 (Figures 2B and 2C) for the two source angles θ_0 clearly illustrates the presence of an inversion in the sign of $\Delta A_{\epsilon,\epsilon}$ as θ_0 is rotated by 180° , which is consistent with equation (8.1) where $\Delta A_{\epsilon,\epsilon}(\theta_0 + \pi) = -\Delta A_{\epsilon,\epsilon}(\theta_0)$. Previous observations of inversion in the sign of far-field chiroptical response due to θ_0 rotation suggest an absence of optical activity in the underlying medium (21, 30), verifying our observations; whereas the lack of sign change in the $\Delta A_{\Gamma,\epsilon}$ due to θ_0 rotation, where $\Delta A_{\Gamma,\epsilon}(\theta_0 + \pi) = \Delta A_{\Gamma,\epsilon}(\theta_0)$, is indicative of optical activity (30). The total response, ΔA , plotted for $\theta_0 = 0^\circ$ and $\theta_0 = 180^\circ$ exhibits an asymmetric spectral lineshape due to the competing contributions from the $\Delta A_{\epsilon,\epsilon}$ response, which exhibits a single-fold symmetric lineshape, and the $\Delta A_{\Gamma,\epsilon}$ response, which exhibits a two-fold symmetric lineshape (Figure 2D), indicating the presence of both CO_{OA} and CO_{abs} in the total chiroptical response.

Analogous to the dependence of $\Delta A_{\epsilon,\epsilon}$ and $\Delta A_{\Gamma,\epsilon}$ responses on θ_0 , further insight can be achieved by analyzing the dependence of the chiroptical response on the azimuth angle ϕ_0 (for any θ_0 , except at $\theta_0 = 0^\circ$ and 180° where ϕ_0 is undefined). For an identical configuration of Figure 2A, $\Delta A_{\epsilon,\epsilon}$ and $\Delta A_{\Gamma,\epsilon}$ plotted vs. incident wavelength λ_0 (Figure 2E-G) for two source azimuth angles $\phi_0 = 0^\circ$ and 180° (at $\theta_0 = 45^\circ$) illustrates the presence of an inversion in the sign of $\Delta A_{\Gamma,\epsilon}$ instead, as ϕ_0 is rotated by 180° . This follows from equations (8.1-8.2) where $\Delta A_{\epsilon,\epsilon}(\phi_0 + \pi) = \Delta A_{\epsilon,\epsilon}(\phi_0)$ and $\Delta A_{\Gamma,\epsilon}(\phi_0 + \pi) = -\Delta A_{\Gamma,\epsilon}(\phi_0)$, respectively. This inversion in the $\Delta A_{\Gamma,\epsilon}$ response can be further described by assuming $d_{1,z} = d_{2,z} = 0 \text{ nm}$ to make a two-dimensional structure wherein the spatial dispersion dependence $\vec{k} \cdot (\delta\vec{r}_1 - \delta\vec{r}_2)$ of equation (8.2) simplifies to $kd \sin \theta_0 (\sin \phi_0 - \cos \phi_0)$, for the two oscillators located equidistant from the origin ($d = d_{1,y} = d_{2,x}$), demonstrating the dependence of $\Delta A_{\Gamma,\epsilon}$ on ϕ_0 .

In addition to the dependence of CO response on excitation direction, θ_0 and ϕ_0 , we analyze its dependence on various oscillator parameters including the angular orientation between the two oscillators along the x - y plane, by varying angle ϕ_2 at $\phi_1 = 90^\circ$, and the difference between coupling terms $\zeta_{2,1}(\omega) -$

$\zeta_{1,2}(\omega)$, oscillator frequencies $\Delta\omega = \omega_1 - \omega_2$ and damping coefficients $\Delta\gamma = \gamma_1 - \gamma_2$. For this analysis, we assume the light to be normally incident ($\theta_0 = 0^\circ$) on the two Au nanocuboids, of lengths l_1 and l_2 , that are aligned parallel to the x - y plane with $d_{1,y} = l_1$, $d_{2,x} = l_2$ and placed in a planar arrangement with $d_{1,z} = d_{2,z} = 0$ nm. In such a planar configuration at normal incidence, $\vec{k} \cdot (\delta\vec{r}_1 - \delta\vec{r}_2) = 0$, resulting in $\Delta A_{\Gamma,\epsilon} = 0$ (equation 8.2). Finally, by setting the two resonant wavelengths to be $\lambda_1 = 750$ nm and $\lambda_2 = 735$ nm (corresponding to $\Delta\omega/\gamma = 0.42$), and assuming $\zeta_{1,2}(\omega) = \zeta_{2,1}(\omega)$, the dependence of $\Delta A_{\epsilon,\epsilon}$ on ϕ_2 exhibits a peak response at $\phi_2 = 45^\circ$ (Figure 3A). Note that this observation that a planar two-dimensional plasmonic structure can exhibit a CO_{abs} type chiroptical response, not related to optical activity, is consistent with ref. 30, and is also in agreement with the findings of Eftekhari and Davis (21). In their work, they also note, without explanation, an experimental finding of a peak CO response occurring at $\phi_2 = 52^\circ$ rather than the expected $\phi_2 = 45^\circ$. A simple inclusion of a non-zero coupling difference, $\zeta_{2,1} - \zeta_{1,2}$, between the two oscillators in the model accounts for this behavior wherein by plotting ϕ_2 that maximizes $\Delta A_{\epsilon,\epsilon}$ response as a function of $\zeta_{2,1} - \zeta_{1,2}$ at $\omega = 2.43 \times 10^{15} \text{ s}^{-1}$ (Figure 3B), we show that the presence of asymmetric oscillator coupling causes the maximum peak to occur at values other than $\phi_2 = 45^\circ$. $\Delta A_{\epsilon,\epsilon}$ response can also be maximized by optimizing the oscillator frequencies wherein for $\zeta_{1,2} - \zeta_{2,1} = -5.2 \times 10^{28} \text{ s}^{-2}$ corresponding to $\phi_2 = 52^\circ$, the model also predicts a peak $\Delta A_{\epsilon,\epsilon}$ for $\Delta\omega/\gamma = 0.74$ (Figure 3C). This includes the underlying dependence of the multiplication factor $\kappa(\omega)$ on the difference between the normalized oscillator frequencies $\Delta\omega/\gamma$ (Supplementary Figure S2). Finally, the model predicts a CO response for light normally incident on a geometrically achiral system if asymmetric absorption is present ($\gamma_1 \neq \gamma_2$) – a scenario easily achieved by simply depositing two different metal types for each of the cuboids (Figure 3D). Using dissimilar metals to achieve inhomogeneous damping on a geometrically achiral structure has been shown to exhibit a CO response (33).

Finally, we verify the validity of our generalized model by applying it to the structure and excitation conditions studied using the Born Kuhn model in ref. 20. We assume the two Au nanocuboids in Figure 2A to be of equal lengths (l), aligned orthogonal to each other ($\phi_1 = 90^\circ$ and $\phi_2 = 0^\circ$) with $d_{1,y} = d_{2,x} = l/2$

and separated by a distance d_z along the z -direction, resulting in $\omega_1 = \omega_2 = \omega$, and $\Omega_1 = \Omega_2 = \Omega$ (Supplementary Figure S3A). Note that, for consistency, the cuboid lengths l were scaled to shift the resonance wavelengths to $\lambda_1 = \lambda_2 = 1300$ nm. Illumination of the structure at normal incidence, $\theta_0 = 0^\circ$, under these conditions results in $\Delta A_{\epsilon,\epsilon} = 0$ (from equation 8.1). Also, as expected, due to this lack of CO_{abs} contribution, $\Delta A = \Delta A_{\Gamma,\epsilon}$ plotted vs. incident wavelength λ_0 (Supplementary Figure S3B) exhibits a two-fold symmetric lineshape, and is consistent with the results of ref. 20. Moreover, by applying the geometrical and oscillator parameters to the configuration of supplementary Figure S2A, one could calculate the reduced dielectric and non-locality tensor elements (Supplementary Section S6). Applying these to equation (6.2) and plotting the resulting $\Delta A_{\Gamma,\epsilon}$ vs. λ_0 results in the same response (Supplementary Figure S3B) confirming the predictions of our generalized model as well as its consistency with the Born Kuhn model (20).

Experimental Results

The model described above provides a comprehensive theoretical framework to study the origin and characteristics of various chiroptical response types in both two and three-dimensional optical media under arbitrary excitation conditions. A common performance metric associated with far-field chiroptical measurements is circular diattenuation (CDA), a normalized form of CO response expressed as $\text{CDA} = (T_{RCP} - T_{LCP}) / (T_{RCP} + T_{LCP})$. CDA also corresponds to the **normalized** m_{14} element of the Mueller matrix, so it can be directly extracted from spectroscopic ellipsometry measurements (34). **Note that Mueller matrix spectroscopy also presents an accurate method for distinguishing between the CO_{OA} and CO_{abs} contributions in a far-field chiroptical measurement, however this requires measurement of both m_{14} and m_{41} elements (17).** As shown below, we verify through model calculations that both CDA and ΔA represent the same optical phenomenon – hence for the simplicity of analysis, we present the following experimental measurements and comparisons with model predictions in the CDA format. Note that an alternate metric based on measuring optical chirality flux has recently been proposed as a quantitative far-field observable

of the magnitude and handedness of the near-field chiral density in a nanostructured optical medium (35). Measured using a technique referred to as chirality flux spectroscopy, it corresponds to the third Stokes parameter which is directly related to the degree of circular polarization of the scattered light in the far-field (36), and carries information of the chiral near-fields. For the purposes of discussions in this manuscript, and its consistency with existing literature, we limit our analysis to measurements using the more prevalent metric of CO (or equivalently CDA) obtained from traditional CD spectroscopic measurements.

We experimentally characterize three planar cuboid configurations (Figure 4A, left column), by measuring their far-field CDA response, under various excitation conditions, and compare them to predictions of the model. Respective expressions for $\Delta A_{\epsilon,\epsilon}$ and $\Delta A_{\Gamma,\epsilon}$ in the three configurations, assuming $d_{1,z} = d_{2,z} = 0$ nm and $\gamma_1 = \gamma_2 = \gamma$ (equations 8.1 and 8.2), are listed in Figure 4A, right column. Note that $\vec{k} \cdot (\delta\vec{r}_1 - \delta\vec{r}_2)$ term in these planar configurations simplifies to $kd \sin \theta_0 (\sin \phi_0 - \cos \phi_0)$. The devices, consisting of an array of two Au nanocuboids (thickness $t = 40$ nm) of varying lengths (l_1 and l_2) and alignments (varying ϕ_2 at $\phi_1 = 90^\circ$), were fabricated on a fused-silica substrate using electro-beam-lithography and lift-off (see Material and Methods, and Supplementary Section S7). The pitch of the array ($p = 375$ nm) was chosen to minimize coupling between adjacent bi-oscillator unit-cells. The devices were characterized using a spectroscopic ellipsometer between free-space wavelengths of $\lambda_0 = 500$ nm and 1000 nm, under illumination at $\theta_0 = 45^\circ$ for various azimuth angles ϕ_0 (see Material and Methods). The first device consisted of the two Au nanocuboids arranged orthogonal to each other ($\phi_1 = 90^\circ$ and $\phi_2 = 0^\circ$), and were designed to be of different lengths ($l_1 = 120$ nm and $l_2 = 100$ nm placed at $d_{1,y} = d_{2,x} = 100$ nm respectively). Since l_1 and l_2 determines both the resonant frequencies (ω_1 and ω_2) as well as the cross-coupling strengths ($\zeta_{1,2}$ and $\zeta_{2,1}$), setting $l_1 \neq l_2$ constitutes a general configuration where both $\Delta A_{\epsilon,\epsilon}$ and $\Delta A_{\Gamma,\epsilon}$ type contributions can be present in a single CDA measurement. The corresponding CDA spectra (Figure 4B) measured at $\phi_0 = 0^\circ, 90^\circ$, and 135° (blue plots), and at 180° offset from these angles (red plots) clearly show an inversion in the sign, indicating the response to primarily result from $\Delta A_{\Gamma,\epsilon}$. However,

note that the CDA measurements at these angles slightly lack the two-fold symmetry in the spectral lineshape, a result of a minor $\Delta A_{\epsilon,\epsilon}$ contribution. For $\phi_0 = 45^\circ$ and 225° , the spectra lack the sign inversion indicating the response be primarily result from $\Delta A_{\Gamma,\epsilon}$, which also follows from Figure 4A where $\Delta A_{\Gamma,\epsilon} = 0$ at these two ϕ_0 angles. This result is further validated by fabricating a device consisting of Au nanocuboids of equal lengths ($l_1 = l_2 = 120$ nm) wherein the CDA spectra at $\phi_0 = 45^\circ$ and 225° shows no chiroptical response, since both $\Delta A_{\Gamma,\epsilon} = \Delta A_{\epsilon,\epsilon} = 0$, confirming the predictions of the model (Figure 4A). Moreover, by setting $l_1 = l_2$, the two-fold symmetry in the CDA lineshape at $\phi_0 = 0^\circ$ (180°), 90° (270°), and 135° (315°) is recovered, indicating the response to now only consist of $\Delta A_{\Gamma,\epsilon}$ contribution, a signature of optical activity (Figure 4C). Hence, it is possible for a geometrically achiral structure to exhibit optical activity under certain illumination conditions. **It follows then due to reciprocity that optical activity may be detectable at large scattering angles when a source field is normally incident on a planar achiral structure. This phenomenon was recently confirmed by Kuntman *et al.* using a scattering matrix decomposition method (37).** Note that the similarity between the calculated CDA and ΔA response (plotted under the conditions of Figure 4B, supplementary Figure S5) verifies our assumption that they are equivalent measurements, and can be used interchangeably.

For a device with Au nanocuboids of equal lengths $l_1 = l_2 = 120$ nm, aligned parallel to each other ($\phi_1 = 90^\circ$ and $\phi_2 = 90^\circ$), equations (8.1 and 8.2) predict both $\Delta A_{\epsilon,\epsilon}$ and $\Delta A_{\Gamma,\epsilon}$ to be zero, under illumination at $\theta_0 = 45^\circ$ for any ϕ_0 . Consistent with these predictions, while the CDA spectra measured at $\phi_0 = 0^\circ$ (180°) and 90° (270°) shows no response, however, the spectra at $\phi_0 = 45^\circ$ (225°) and 135° (315°) shows a pronounced signal of the $\Delta A_{\epsilon,\epsilon}$ type (no sign inversion for ϕ_0 rotation by 180° , Figure 4D). We attribute this phenomenon to originate from coupling to the optical resonances (\vec{u}'_1 and \vec{u}'_2) along the cuboid widths ($w_1 = w_2 = 60$ nm), acting as additional orthogonally oriented oscillators in the system, resulting in a two-dimensional anisotropic optical system supporting two orthogonal elliptical eigenmodes (30). A circularly polarized light at non-normal incidence ($\theta_0 \neq 0^\circ$ and 180°) projects an elliptically polarized field along the plane of the device (red ellipse, Figure 5A-D), which at certain azimuth angles ϕ_0

can access these elliptical eigenmodes (dashed yellow ellipses, Figure 5A-D). At $\phi_0 = 0^\circ$ (180°) or $\phi_0 = 90^\circ$ (270°), both orthogonal eigenmodes are accessed equally resulting in the total chiroptical response to be zero; whereas, at $\phi_0 = 45^\circ$ (225°) and 135° (315°) only one of the two eigenmodes can be excited resulting in a strong CDA response. This dependence of peak $|\Delta A_{\epsilon,\epsilon}|$ on the azimuth angle ϕ_0 is shown schematically in Figure 5E. These results are also consistent with Figure 5F, which follows from equations (8.1) and (8.2), wherein incorporation of contributions from these additional oscillators results in a zero $\Delta A_{\Gamma,\epsilon}$ response, whereas $\Delta A_{\epsilon,\epsilon}$ response is shown to stay proportional to $(\zeta_{1',2} - \zeta_{2,1'})$. Note that for the CDA calculations in Figure 4B and 4C, only coupling between the oscillators along their long-axis (\vec{u}_1 and \vec{u}_2) was assumed. Absence of contributions from coupling between the oscillators along their short-axis, \vec{u}'_1 and \vec{u}'_2 , in the calculations could explain the minor discrepancy between the calculated and experimentally measured CDA spectra.

In addition, it is instructive to study the CO response of a device where the two Au nanocuboids of equal lengths are aligned such that $\phi_1 = 90^\circ$ and $\phi_2 = 45^\circ$ in a planar arrangement. Upon illumination of this structure at $\theta_0 = 45^\circ$ for various ϕ_0 , the measured CDA response neither shows any clear inversion in sign with 180° rotation of ϕ_0 , nor any apparent symmetry in the spectral lineshape (Supplementary Figure S6). This is because the various sub-oscillators (\vec{u}_1 , \vec{u}_2 , \vec{u}'_1 and \vec{u}'_2) in this system are aligned with respect to each other such that they can all be inter-coupled, resulting in both $\Delta A_{\Gamma,\epsilon}$ and $\Delta A_{\epsilon,\epsilon}$ contributions to be significant. This serves as a simple example for a system where the measured far-field CO response is ambiguous, and its underlying origin can be difficult to interpret.

Finally, until now we have applied the model predictions to, and validated them against, existing literature and experimental CDA measurements on planar metallic nanocuboid oscillators. However, as mentioned earlier, a strong far-field CO response of the CO_{axial} type has been observed in an all-dielectric metamaterial acting as a uniaxial or a biaxial medium wherein symmetry breaking of the unit cell along the direction of source propagation enables asymmetric transmission of the two CP components of incident linearly polarized light (19, 24, 25). An additional deployment of geometric phase further enables

independent phase-front manipulation of these two components (24, 38). We demonstrate the generality of the model by applying it to an all-dielectric optical medium with a mirror-symmetry breaking chiral unit cell that enables asymmetric transmission of the two CP components, but without a geometric phase (Supplementary Section S10), and illustrate the conditions under which the Poynting vectors associated with the LCP and RCP components of a linearly polarized (LP) light normally incident on an all-dielectric biaxial medium can propagate in different directions within the medium. A simple spatial filtering of either the LCP or the RCP on the exit side can result in a strong CO response, as shown in ref. 25. Note that such a far-field CO response is not related to optical activity.

Discussion

In conclusion, we have developed a comprehensive analytical model to study the microscopic origin of chiroptical response in optical media. Closed-form expressions for the various microscopic phenomena governing the far-field CO response is shown to provide intuitive insights when systematically studied for various sample geometries and optical excitation conditions. Optical activity, CO_{OA} , characterized in the far-field by spectrally shifted transmission (or reflection) curves due to the accessibility of RCP and LCP light to hybridized eigen-modes, is shown to originate at the microscopic scale when coupled oscillators are spatially separated along the direction of source propagation. Differential absorption, CO_{abs} , another CO response type unrelated to optical activity is characterized in the far-field by amplitude shifted transmission (or reflection) curves due to the presence of distinct near-field absorption modes for RCP and LCP light. CO_{abs} is shown to occur when the oscillators, in the presence of loss, are angularly separated along the direction of source electric-field rotation. The third CO response type, CO_{axial} , is characterized in the far-field by the spatial separation of RCP and LCP light. CO_{axial} is shown to occur when the Poynting vectors associated with the characteristic RCP and LCP waves of a biaxial medium are angularly offset. Both analytical and experimental methods provided here suggest a simple method for identifying the presence of, and distinguishing between, these various CO response types. As engineered chiral optical media becomes an essential component of advanced technologies such as enhanced CD spectroscopy,

identification of the microscopic behavioral differences in the far-field optical response have become increasingly crucial. The generalized theoretical framework presented here is expected to aid in the application-specific design and study of engineered chiroptical systems.

Materials and Methods

Device Fabrication. The Au nanocuboid structures are fabricated on 500 μm thick fused-silica substrates. 100 nm thick poly-methyl methacrylate (PMMA) resist was spun-coated on the substrates, followed by deposition of 20 nm Al film using thermal evaporation as an anti-charging layer. Electron-beam lithography at 100 keV was then used to expose the nanocuboid patterns. After exposure, the Al layer was removed using a 60 s bath in a tetramethylammonium hydroxide (TMAH) based developer followed by a 30 s rinse in deionized water. PMMA was developed for 90 s in methyl isobutyl ketone (MIBK) followed by a 30 s rinse in isopropyl alcohol (IPA). Electron beam (E-beam) evaporation was used to deposit a 2 nm thick Ti adhesion layer, followed by a 40 nm thick Au-film. A twelve-hour soak in acetone was used for lift-off, revealing the completed cuboid structures on the substrate surface. The fabrication steps are schematically outlined in Supplementary Figure S4.

Optical Characterization. For experimental characterization, the samples were illuminated from free-space at wavelengths between $\lambda_0 = 500$ nm to 1000 nm at a fixed angle $\theta_0 = 45^\circ$ for various source azimuth angles ϕ_0 . The incident light was focused on the sample to a spot-size (along the long-axis) of ≈ 400 μm , and the incident polarization was controlled using an achromatic waveplate. The CDA spectra was directly measured, using a spectroscopic ellipsometer in reflection mode, by extracting the m_{14} element of the Mueller matrix.

Supplementary Materials

Supplementary Sections S1–S10

Fig. S1. Arrangement of bi-oscillator molecular unit-cells in a representative volume of optical media.

Fig. S2. Dependence of the multiplication factor κ on the difference between oscillator frequencies.

Fig. S3. Chiroptical response of orthogonally oriented identical nanocuboids in a three-dimensional arrangement.

Fig. S4. Nanofabrication process steps.

Fig. S5. Comparison between calculated CDA and ΔA spectral response.

Fig. S6. Experimental measurements of the chiroptical response of 45° oriented cuboids of equal lengths.

Fig. S7. Isofrequency surfaces and Poynting vectors for the eigenmodes of a biaxial medium.

References and Notes

1. D. G. Blackmon, The origin of biological homochirality, *Philosophical Transactions B* **366**, 2878-2884 (2011).
2. J. M. Dreiling and T. J. Gay, Chirally sensitive electron-induced molecular breakup and the Vester-Ulbricht hypothesis, *Physical Review Letters* **113**, 118103 (2014).
3. J. C. Aponte, J. E. Elsila, D. P. Glavin, S. N. Milam, S. B. Charnley, and J. P. Dworkin, Pathways to meteoritic glycine and methylamine, *ACS Earth and Space Chemistry* **1**, 3-13 (2017).
4. J. M. Brown and S. G. Davies, Chemical asymmetric synthesis, *Nature* **342**, 631-636 (1989).
5. Y. Wang, Q. Han, Q. Zhang, Y. Huang, L. Guo, and Y. Fu, Chiral recognition of penicillamine enantiomers based on a vancomycin membrane electrode, *Analytical Methods* **5**, 5579 (2013).
6. D. Leung and E. V. Anslyn, Rapid determination of enantiomeric excess of α -chiral cyclohexanones using circular dichroism spectroscopy, *Organic Letters* **13**, 2298-2301 (2011).
7. S. W. Smith, Chiral toxicology: It's the same thing ... only different, *Toxicological Sciences* **110**, 4-30 (2009).
8. M. Budau, G. Hancu, A. Rusu, M. Carcu-Dobrin and D. L. Muntean, Chirality of modern antidepressants: An overview, *Advanced Pharmaceutical Bulletin* **7**, 495-500 (2017).
9. D. W. Green, J. M. Lee, E. J. Kim, D. J. Lee and H. S. Jung, Chiral biomaterials: From molecular design to regenerative medicine, *Advanced Materials Interfaces* **3**, 1500411 (2016).
10. A. K. Visheratina, F. Purcell-Milton, R. Serrano-Garcia, V. A. Kuznetsova, A. O. Orlova, A. V. Fedorov, A. V. Baranov, and Y. K. Gun'ko, Chiral recognition of optically active CoFe_2O_4 magnetic nanoparticles by CdSe/CdS quantum dots stabilised with chiral ligands, *Journal of Materials Chemistry C* **5**, 1692 (2017).
11. N. J. Greenfield, Using circular dichroism spectra to estimate protein secondary structure, *Nature Protocols* **1**, 2876-2890 (2006).
12. B. Ranjbar and P. Gill, Circular dichroism techniques: Biomolecular and nanostructural analysis – a review, *Chemical Biology & Drug Design* **74**, 101-120 (2009).
13. V. Bellotti and M. Stoppini, Protein misfolding diseases, *The Open Biology Journal* **2**, 228-234 (2009).
14. N. Abdulrahman, Z. Fan, T. Tonooka, S. Kelly, N. Gadegaard, E. Hendry, A. O. Govorov, and M. Kadodwala, Induced chirality through electromagnetic coupling between chiral molecular layers and plasmonic nanostructures, *Nano Letters* **12**, 977 (2012).
15. M. L. Nesterov, X. Yin, M. Schäferling, H. Giessen, and T. Weiss, The role of plasmon-generated near fields for enhanced circular dichroism spectroscopy, *ACS Photonics* **3**, 578-583 (2016).
16. P. L. Polavarapu, Kramers-Kronig transformation for optical rotary dispersion studies, *The Journal of Physical Chemistry A* **109**, 7013-7023 (2005).

17. O. A. Barriel, Mueller matrix polarimetry of anisotropic chiral media, Ph.D. Thesis, Universitat de Barcelona (2010).
18. H. Wang, Z. Li, H. Zhang, P. Wang, and S. Wen, Giant local circular dichroism within an asymmetric plasmonic nanoparticle trimer, *Scientific Reports* **5**, 8207 (2015).
19. J. Hu, X. Zhao, Y. Lin, A. Zhu, X. Zhu, P. Guo, B. Cao, and C. Wang, All-dielectric metasurface circular dichroism waveplate, *Scientific Reports* **7**, 41893 (2017).
20. X. Yin, M. Schäferling, B. Metzger and H. Giessen, Interpreting chiral nanophotonic spectra: The plasmonic Born-Kuhn model, *Nano Letters* **13**, 6238-6243 (2013).
21. F. Eftekhari and T. J. Davis, Strong chiral optical response from planar arrays of subwavelength metallic structures supporting surface plasmon resonances, *Physical Review B* **86**, 075428 (2012).
22. A. F. Najafabadi and T. Pakizeh, Optical absorbing origin of chiroptical activity in planar plasmonic metasurfaces, *Scientific Reports* **7**, 10251 (2017).
23. A. B. Khanikaev, N. Arju, Z. Fan, D. Purtseladze, F. Lu, J. Lee, P. Sarriugarte, M. Schnell, R. Hillenbrand, M. A. Belkin and G. Shvets, Experimental demonstration of the microscopic origin of circular dichroism in two-dimensional metamaterials, *Nature Communications* **7**, 12045 (2016).
24. Z. Ma, Y. Li, Y. Li, Y. Gong, S. A. Maier, and M. Hong, All-dielectric planar chiral metasurface with gradient geometric phase, *Optics Express* **26**, 6067-6078 (2018).
25. A. Y. Zhu, W. T. Chen, A. Zaidi, Y. W. Huang, M. Khorasaninejad, V. Sanjeev, C. W. Qiu, and F. Capasso, Giant intrinsic chiro-optical activity in planar dielectric nanostructures, *Light: Science & Applications* **7**, 17158 (2018).
26. X. Lan, X. Lu, C. Shen, Y. Ke, W. Ni, and Q. Wang, Au nanorod helical superstructures with designed chirality, *Journal of the American Chemical Society* **137**, 457-462 (2015).
27. S. Zu, Y. Bao, and Z. Fang, Planar plasmonic chiral nanostructures, *Nanoscale* **8**, 3900-3905 (2016).
28. A. F. Najafabadi and T. Pakizeh, Analytical chiroptics of 2D and 3D nanoantennas, *ACS Photonics* **4**, 1447-1452 (2017).
29. Y. P. Svirko and N. I. Zheludev, *Polarization of light in nonlinear optics*, Wiley-VCH, New York (1998).
30. V. A. Fedotov, P. L. Mladyonov, S. L. Prosvirnin, A. V. Rogacheva, Y. Chen and N. I. Zheludev, Asymmetric propagation of electromagnetic waves through a planar chiral structure, *Physical Review Letters* **97**, 167401 (2006).
31. M. Schäferling, *Chiral nanophotonics: Chiral optical properties of plasmonic systems*, Springer (2017).
32. N. Liu, H. Guo, L. Fu, S. Kaiser, H. Schweizer and H. Giessen, Three-dimensional photonic metamaterials at optical frequencies, *Nature Materials* **7**, 31-37 (2008).

33. P. Banzer, P. Wozniak, U. Mick, I. De Leon and R. W. Boyd, Chiral optical response of planar symmetric nanotrimers enabled by heteromaterial selection, *Nature Communications* **7**, 13117 (2016).
34. R. A. Chipman, *Mueller matrices. Polarimetry, Handbook of Optics, Volume 1: Geometrical and physical optics, polarized light, components and instruments, 3rd ed.*, McGraw-Hill (2010).
35. L. V. Poulikakos, P. Thureja, A. Stollmann, E. De Leo, and D. J. Norris, Chiral light design and detection inspired by optical antenna theory, *Nano Letters* **8**, 4633–4640 (2018).
36. J. D. Jackson, *Classical Electrodynamics, 3rd ed.*, John Wiley & Sons (1999).
37. M. A. Kuntman, E. Kuntman, J. Sancho-Parramon and O. Arteaga, Light scattering by coupled oriented dipoles: Decomposition of the scattering matrix, *Physical Review B* **98**, 045410 (2018).
38. X. Chen, Z. Tao, C. Chen, C. Wang, L. Wang, H. Jiang, D. Fan, Y. Ekinici, and S. Liu, All-dielectric metasurfaces-based roll-angle sensor, *Sensors and Actuators A* **279**, 509-517 (2018).
39. L. Novotny and B. Hecht. *Principles of Nano-Optics, 2nd ed.*, Cambridge University Press (2012).
40. J. A. Kong, *Electromagnetic Wave Theory*, EMW Publishing (2005).

Acknowledgments

Funding: M. S. D., W. Z., and A. A. acknowledge support under the Cooperative Research Agreement between the University of Maryland and the National Institute of Standards and Technology, Center for Nanoscale Science and Technology, Award#70NANB14H209, through the University of Maryland.

Author contributions: The experiments were designed and performed by M. S. D., W. Z. and A. A. Simulations were performed by M. S. D. with further analysis by W. Z., J. K. L., H. J. L. and A. A. Device fabrication and characterization was performed by M. S. D. and W. Z. All authors contributed to the interpretation of results and participated in manuscript preparation.

Competing interests: The authors declare that they have no competing interests.

Data and materials availability: All data needed to evaluate the conclusions in the paper are present in the paper and/or the Supplementary Materials. Additional data available from authors upon request.

Figure Captions

Fig. 1. Generalized coupled oscillator model space. (A) Representation of an arbitrarily oriented incident plane-wave of wavevector $\vec{k} = -k(\hat{a}_x \sin \theta_0 \cos \phi_0 + \hat{a}_y k \sin \theta_0 \sin \phi_0 + \hat{a}_z k \cos \theta_0)$ originating from a source placed at infinity. (B) A molecular unit-cell consisting of two oscillators \vec{u}_1 and \vec{u}_2 located at distances δr_1 and δr_2 , respectively from the molecular center of mass, O' , which is located at a distance \vec{r}_0 from the origin O . Each oscillator is arbitrarily oriented with respect to the other. (C) Coordinate system with the origin (O') corresponding to the molecular center of mass. The oscillator displacement from O' is given by $\delta \vec{r}_i = \delta r_i(\hat{a}_x \sin \xi_i \cos \psi_i + \hat{a}_y \sin \xi_i \sin \psi_i + \hat{a}_z \cos \xi_i)$ for $i = 1, 2$. (D) The origin here corresponds to oscillator center of mass (O'') which is positioned at a distance $\delta \vec{r}_i$ from the molecular center of mass (O'). The orientation of each oscillator is described by the unit vector $\hat{u}_i = \hat{a}_x \sin \theta_i \cos \phi_i + \hat{a}_y \sin \theta_i \sin \phi_i + \hat{a}_z \cos \theta_i$ for $i = 1, 2$.

Fig. 2. Dependence of the chiroptical response of nanocuboid bi-oscillator system on source angles θ_0 and ϕ_0 . (A) Relative orientation of the incident light of wavevector \vec{k} with respect to the two nanocuboid oscillators. The two oscillators, represented by \vec{u}_1 and \vec{u}_2 , are oriented parallel to the x - y plane ($\theta_1 = \theta_2 = \pi/2$) with azimuth angles $\phi_1 = 90^\circ$ and $\phi_2 = 45^\circ$, respectively. The nanocuboids are located at $d_{1,z} = d_{2,z} = 100$ nm with $d_{1,y} = d_{2,x} = 100$ nm, and for simplicity, $d_{1,x} = d_{2,y} = 0$ nm was assumed. The nanocuboid parameters were chosen such that they exhibit resonance at wavelengths of $\lambda_1 = 750$ nm and $\lambda_2 = 735$ nm respectively, with coupling strengths $\zeta_{1,2}(\omega_1) = \zeta_{2,1}(\omega_2) = 1.6 \times 10^{29} \text{ s}^{-1}$. (B) The calculated $\Delta A_{\epsilon,\epsilon}$ response at source angles $\theta_0 = 0^\circ$ and 180° (note that ϕ_0 is undefined at these values of θ_0) exhibits a one-fold symmetric lineshape, and experiences an inversion in sign when the incident angle is changed from 0° to 180° . (C) The corresponding $\Delta A_{\Gamma,\epsilon}$ response calculated under the same conditions exhibits a two-fold symmetric lineshape, and does not experience an inversion in sign for a θ_0 change from 0° to 180° . (D) The total CO response $\Delta A = \Delta A_{\epsilon,\epsilon} + \Delta A_{\Gamma,\epsilon}$ for the two source angles does not show any symmetry in the spectral lineshape due to the presence of competing contributions from both $\Delta A_{\epsilon,\epsilon}$ and $\Delta A_{\Gamma,\epsilon}$ response types. (E-G) The chiroptical response for the oscillator configuration and orientations in A calculated at $\theta_0 = 45^\circ$ for two azimuth angles $\phi_0 = 0^\circ$ and 180° . (E) The calculated $\Delta A_{\epsilon,\epsilon}$ response does not change sign when the incident angle ϕ_0 is changed from 0° to 180° . (F) The corresponding $\Delta A_{\Gamma,\epsilon}$ response, however, exhibits an inversion in sign for a 180° change in the source azimuth. At these source angles, $\Delta A_{\epsilon,\epsilon}$ exhibits a one-fold symmetric lineshape whereas $\Delta A_{\Gamma,\epsilon}$ is asymmetric. (G) The total CO response $\Delta A = \Delta A_{\epsilon,\epsilon} + \Delta A_{\Gamma,\epsilon}$ also exhibits an asymmetric lineshape due to the presence of both $\Delta A_{\epsilon,\epsilon}$ and $\Delta A_{\Gamma,\epsilon}$ contributions.

Fig. 3. Dependence of the chiroptical response of nanocuboid bi-oscillator system on oscillator parameters. Chiroptical response of the two oscillators, under normal incidence excitation ($\theta_0 = 0^\circ$), oriented parallel to the x - y plane ($\theta_1 = \theta_2 = \pi/2$) and arranged in a planar arrangement with $d_{1,z} = d_{2,z} = 0$ nm and $d_{1,y} = d_{2,x} = 100$ nm. In this planar configuration at normal incidence, $\Delta A_{\Gamma,\epsilon} = 0$. (A) The dependence of $\Delta A = \Delta A_{\epsilon,\epsilon}$ on the angular orientation between the two oscillators in the x - y plane calculated by varying ϕ_2 at $\phi_1 = 90^\circ$. The oscillators are designed to exhibit resonance at wavelengths of $\lambda_1 = 750$ nm and $\lambda_2 = 735$ nm, and assuming $\zeta_{1,2}(\omega) = \zeta_{2,1}(\omega)$, the peak $\Delta A_{\epsilon,\epsilon}$ response is shown to occur at $\phi_2 = 45^\circ$. (B) The orientation angle of the second oscillator ϕ_2 (at $\phi_1 = 90^\circ$) at which $\Delta A_{\epsilon,\epsilon}$ is maximized for a non-zero difference in coupling coefficients, $\zeta_{1,2} - \zeta_{2,1}$, plotted here at $\omega = 2.43 \times 10^{15} \text{ s}^{-1}$. (C) $\Delta A_{\epsilon,\epsilon}$ dependence on the normalized difference in resonant frequencies $(\Delta\omega)/\gamma$ at $\zeta_{1,2} - \zeta_{2,1} =$

$-5.2 \times 10^{28} \text{ s}^{-2}$ corresponding to $\phi_2 = 52^\circ$. A peak $\Delta A_{\epsilon,\epsilon}$ response is achieved at $(\Delta\omega)/\gamma = 0.74$. **(D)** $\Delta A_{\epsilon,\epsilon}$ dependence at normal incidence on a geometrically achiral system ($l_1 = l_2$) for oscillators of the same metal corresponding to $\gamma_1 = \gamma_2$ (red line), and of dissimilar metals corresponding to $\gamma_1 \neq \gamma_2$ (blue line).

Fig. 4. Experimental characterization of the chiroptical response of two-dimensional planar Au nanocuboids. **(A)** Simplified $\Delta A_{\epsilon,\epsilon}$ and $\Delta A_{\Gamma,\epsilon}$ relations, calculated from equations (8.1) and (8.2), for three planar nanocuboids configurations. **Top row**, The two oscillators are aligned orthogonal to each other ($\phi_1 = 90^\circ$ and $\phi_2 = 0^\circ$) and are assumed to be of different lengths ($l_1 \neq l_2$), corresponding to $\omega_1 \neq \omega_2$ and $\zeta_{1,2}(\omega) \neq \zeta_{2,1}(\omega)$. In such a system, it is expected that both $\Delta A_{\epsilon,\epsilon}$ and $\Delta A_{\Gamma,\epsilon}$ contributions are present. **Middle row**, Same as above except with $l_1 = l_2$ resulting in $\omega_1 = \omega_2 = \omega_0$, $\zeta_{1,2} = \zeta_{2,1}$. In this configuration, $\Delta A_{\epsilon,\epsilon}$ contribution is expected to be absent for excitation at any arbitrary angle of incidence. **Bottom row**, Same as above ($l_1 = l_2$) except that the two oscillators are oriented parallel to each other ($\phi_1 = 90^\circ$ and $\phi_2 = 90^\circ$). Ignoring any optical resonance along the width of the nanocuboid, the model predicts both $\Delta A_{\epsilon,\epsilon}$ and $\Delta A_{\Gamma,\epsilon}$ to be absent, for excitation at any arbitrary angle of incidence. **(B-D)** Corresponding experimental CDA measurements for an array of planar Au nanocuboid bi-oscillators, illuminated with free-space light between wavelengths of $\lambda_0 = 500 \text{ nm}$ and 1000 nm , as a function of incidence angle (varying ϕ_0 at a fixed $\theta_0 = 45^\circ$) for the three configurations shown in **A**. Top-down scanning-electron microscopy (SEM) images of unit-cells consisting of the two Au nanocuboid oscillators, overlaid with the coordinate system and orientation of the in-plane wavevector of the incident light ($\vec{k}_{\parallel xy}$) along the x - y plane, are shown at the top of each column. Scale bar represents 120 nm in the SEM images. **(B)** Experimentally measured (solid lines) and the model calculated (dashed lines) CDA spectra for a sample consisting of Au nanocuboids of unequal lengths ($l_1=120 \text{ nm}$ and $l_2 = 100 \text{ nm}$) oriented orthogonal to each other ($\phi_1 = 90^\circ$ and $\phi_2 = 0^\circ$) at various ϕ_0 . The spectra at $\phi_0 = 0^\circ, 90^\circ$, and 135° (blue plots), and at 180° offset from these angles (solid red plots) show an inversion in the sign, which is absent for excitation at $\phi_0 = 45^\circ$ (225°). The CDA model plots were calculated assuming $\zeta_{2,1}(\omega_1) = 6.4 \times 10^{29} \text{ s}^{-2}$ and $\zeta_{1,2}(\omega_2) = 8.1 \times 10^{29} \text{ s}^{-2}$ at $\lambda_1 = 750 \text{ nm}$ and $\lambda_2 = 720 \text{ nm}$, respectively. **(C)** Equivalent CDA measurements and model calculations for a device with Au nanocuboids of equal lengths ($l_1 = l_2 = 120 \text{ nm}$). As expected, the CDA response is absent from this device for excitation at $\phi_0 = 45^\circ$ (225°). Moreover, the response at other ϕ_0 angles exhibits a two-fold symmetric spectral lineshape (absent from measurements in **B**) indicating the CDA to only result from $\Delta A_{\Gamma,\epsilon}$ contribution. Model parameters used in the calculations are $\zeta_{2,1}(\omega_0) = \zeta_{1,2}(\omega_0) = 8.1 \times 10^{29} \text{ s}^{-2}$ at $\lambda_1 = \lambda_2 = 745 \text{ nm}$. **(D)** Same as **C** except that the two Au nanocuboids are oriented parallel to each other ($\phi_1 = 90^\circ$ and $\phi_2 = 90^\circ$). The CDA spectra at $\phi_0 = 0^\circ$ (180°) and 90° (270°) shows no response whereas the spectra at $\phi_0 = 45^\circ$ (225°) and 135° (315°) shows a pronounced signal of the $\Delta A_{\epsilon,\epsilon}$ type (no sign inversion for ϕ_0 rotation by 180°). The CDA response at latter angles, though not expected from the model predictions in **A**, can be attributed to the coupling to optical resonances along the cuboid widths ($w_1 = w_2 = 60 \text{ nm}$), acting as additional orthogonally oriented oscillators (\vec{u}'_1 and \vec{u}'_2) in the system.

Fig. 5. Origin of the chiroptical response from parallel nanocuboid oscillators through coupling along orthogonal oscillator dimensions. **(A-D)** Top-down SEM images of the device consisting of an array of Au nanocuboid oscillators oriented parallel to each other. Overlaid are the constitutive elliptical eigenmodes (dashed yellow curves) and the projected in-plane source electric field ($\vec{E}_{\parallel xy}$), indicated by a red vector

arrow that traces the red elliptical path for a circularly polarized light at non-normal incidence. Scale bar represents 125 nm in the SEM images. **(A, B)** Orientation of the two eigenmodes relative to the source electric field at $\phi_0 = 0^\circ$ (180°) and 90° (270°) illustrating that they can be accessed equally. **(C, D)** Same as above, except at source azimuths $\phi_0 = 45^\circ$ (225°) and 135° (315°) illustrating that only one of the two eigenmodes can be accessed. **(E)** Dependence of $|\Delta A_{\epsilon,\epsilon}|$ on ϕ_0 for the parallel nanocuboid oscillator configuration studied here. The orientation of the long and short axis oscillators (\vec{u}_i and \vec{u}'_i respectively) corresponding to the length (l_i) and width (w_i) of the two nanocuboids relative to ϕ_0 is shown for clarity. **(F) Top**, Schematic illustrations of the two coupled-oscillator contributions that result in a far-field CO response from parallel nanocuboid oscillators of equal lengths ($l_1 = l_2$) and widths ($w_1 = w_2$) upon illumination at $\theta_0 = 45^\circ$ and $\phi_0 = 45^\circ$ (225°) or 135° (315°). Note that since $\vec{u}_1 = \vec{u}_2$ and $\vec{u}'_1 = \vec{u}'_2$ in this configuration, leads to $\zeta_{1,2} = \zeta_{2,1}$ as well as $\zeta_{1,2'} = \zeta_{2,1'}$ and $\zeta_{2',1} = \zeta_{1',2}$ resulting in $\Delta A_{\epsilon,\epsilon}$ response to be doubled (from equation (8.1), **bottom**). However, because of the inversion of the spatial dispersion term $\vec{k} \cdot (\delta\vec{r}_1 - \delta\vec{r}_2)$ of equation (8.2), the $\Delta A_{\Gamma,\epsilon}$ contributions between these two configurations become equal and opposite, cancelling each other out.

Fig. 1. Generalized coupled oscillator model space.

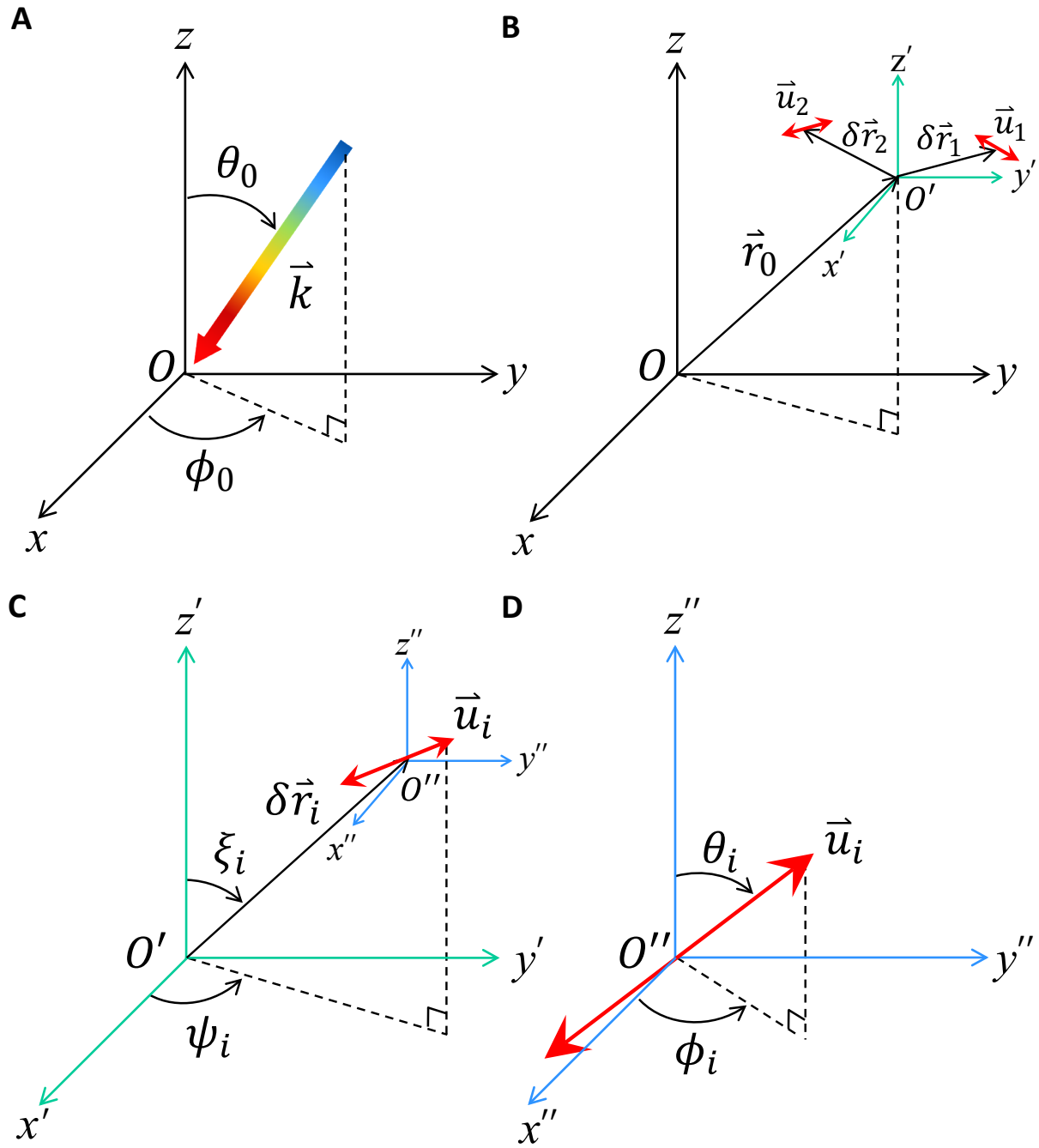


Fig. 2. Dependence of the chiroptical response of nanocuboid bi-oscillator system on source angles θ_0 and ϕ_0 .

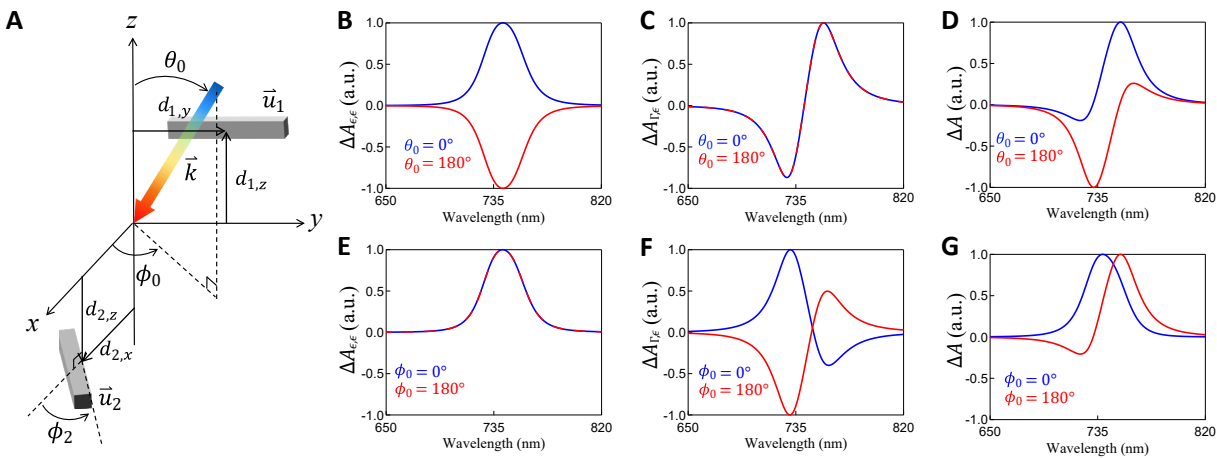


Fig. 3. Dependence of the chiroptical response of nanocuboid bi-oscillator system on oscillator parameters.

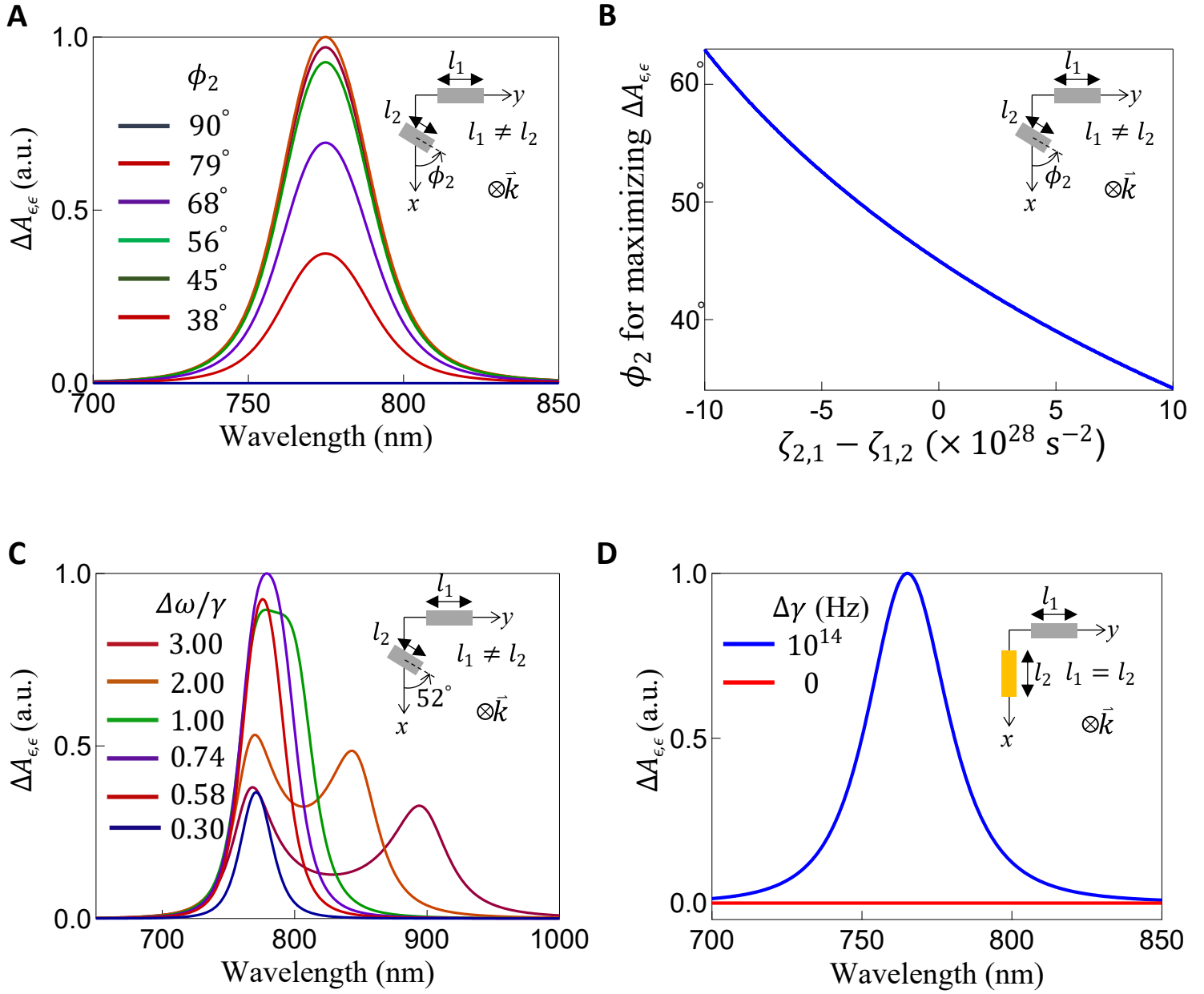


Fig. 4. Experimental characterization of the chiroptical response of two-dimensional planar Au nanocuboids.

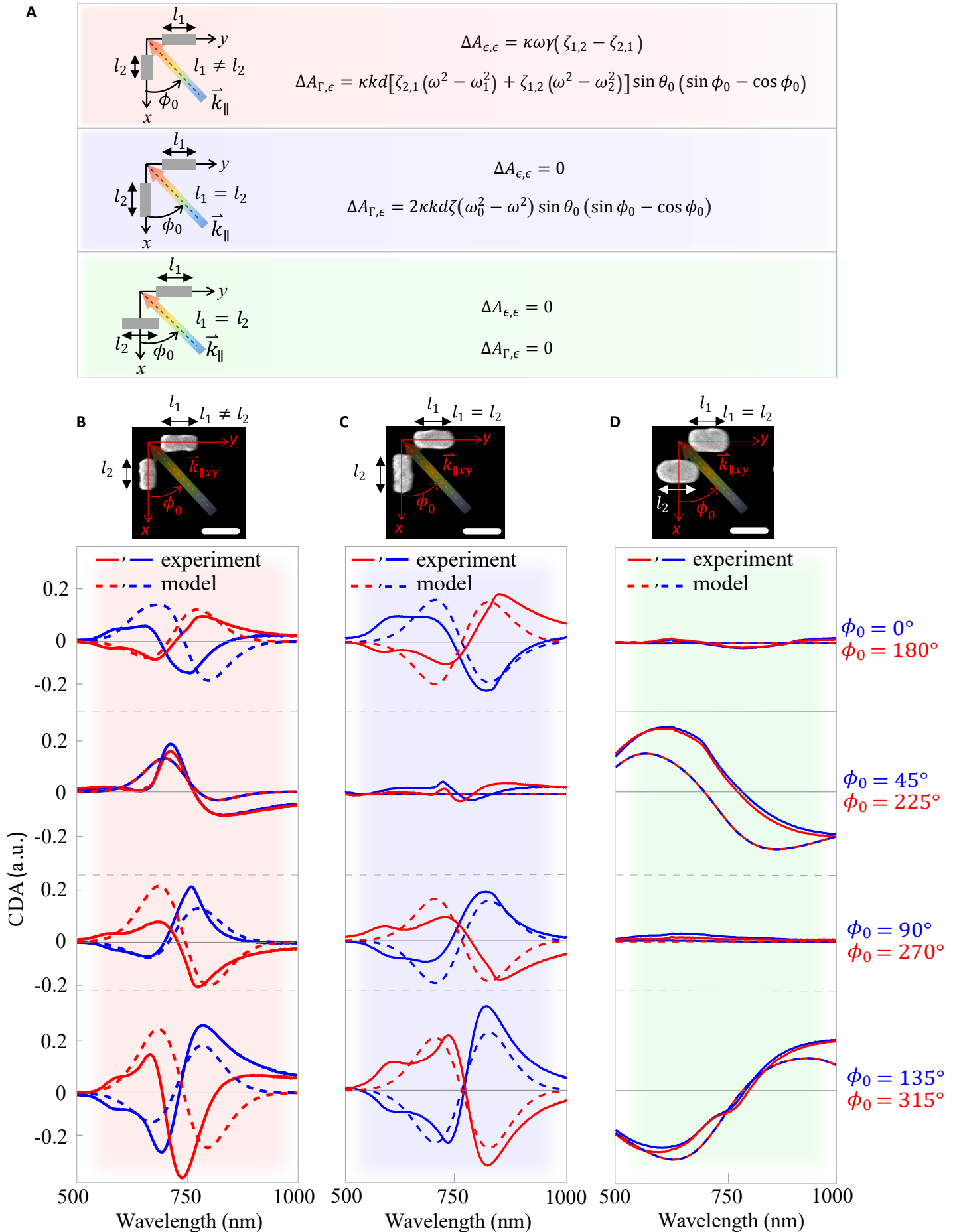
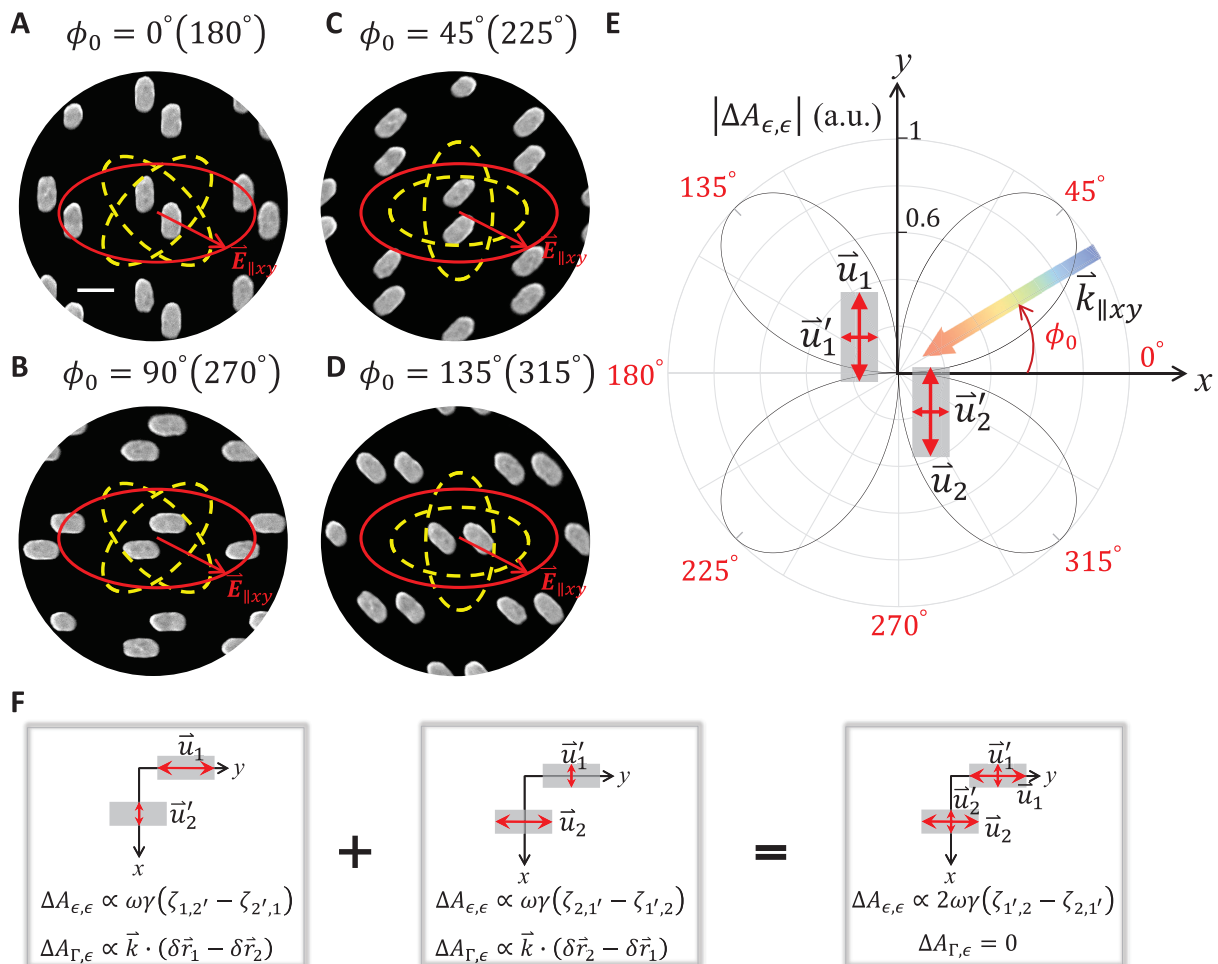


Fig. 5. Origin of the chiroptical response from parallel nanocuboid oscillators through coupling along orthogonal oscillator dimensions.



Supplementary Materials for:

Microscopic origin of the chiroptical response of optical media

Matthew S. Davis^{1, 2, 3*}, Wenqi Zhu^{1, 2}, Jay K. Lee³, Henri J. Lezec¹ and Amit Agrawal^{1, 2*}

¹Center for Nanoscale Science and Technology, National Institute of Standards and Technology, Gaithersburg, MD 20899 USA

²Maryland NanoCenter, University of Maryland, College Park, MD 20742 USA

³Department of Electrical Engineering and Computer Science, Syracuse University, Syracuse, NY 13244 USA

*Corresponding authors: Email: matthew.davis@nist.gov; amit.agrawal@nist.gov

This Supplementary Materials file includes:

Supplementary Sections S1–S10

Fig. S1. Arrangement of bi-oscillator molecular unit-cells in a representative volume of optical media.

Fig. S2. Dependence of the multiplication factor κ on the difference between oscillator frequencies.

Fig. S3. Chiroptical response of orthogonally oriented identical nanocuboids in a three-dimensional arrangement.

Fig. S4. Nanofabrication process steps.

Fig. S5. Comparison between calculated CDA and ΔA spectral response.

Fig. S6. Experimental measurements of the chiroptical response of 45° oriented cuboids of equal lengths.

Fig. S7. Isofrequency surfaces and Poynting vectors for the eigenmodes of a biaxial medium.

Section S1. Generalized coupled oscillator model parameter definitions

The displacement and orientation terms corresponding to the two oscillators \vec{u}_i in cartesian coordinates are shown in Figure 1 of the manuscript. The incident electric field, \vec{E}_0 , can be conveniently defined as the sum of transverse-magnetic (TM) and transverse-electric (TE) components as $\vec{E}_0 = \vec{E}_{TM} + \vec{E}_{TE}$, and expressed individually in cartesian coordinates as:

$$\vec{E}_{TM} = E_{TM}(-\hat{a}_x \cos \theta_0 \cos \phi_0 - \hat{a}_y \cos \theta_0 \sin \phi_0 + \hat{a}_z \sin \theta_0) \quad (\text{S1})$$

$$\vec{E}_{TE} = E_{TE}(\hat{a}_x \sin \phi_0 - \hat{a}_y \cos \phi_0) \quad (\text{S2})$$

Here, E_{TM} and E_{TE} are the magnitudes of the TM and the TE components, respectively. Inserting equations (S1-S2) into \vec{E}_0 gives $\vec{E}_0 = \hat{a}_x(-E_{TM} \cos \theta_0 \cos \phi_0 + E_{TE} \sin \phi_0) + \hat{a}_y(-E_{TM} \cos \theta_0 \sin \phi_0 - E_{TE} \cos \phi_0) + \hat{a}_z E_{TM} \sin \theta_0$.

The coupled differential equations (1.1-1.2) of the manuscript are solved by inserting the time harmonic expressions $\vec{u}_1(t) = \hat{u}_1 u_1 e^{-i\omega t}$ and $\vec{u}_2(t) = \hat{u}_2 u_2 e^{-i\omega t}$ resulting in:

$$-\omega^2 u_1 - i\omega\gamma_1 u_1 + \omega_1^2 u_1 + \zeta_{2,1} u_2 = -\frac{e}{m^*} (\vec{E}_0 \cdot \hat{u}_1) e^{i\vec{k} \cdot \vec{r}_1} \quad (\text{S2.1})$$

$$-\omega^2 u_2 - i\omega\gamma_2 u_2 + \omega_2^2 u_2 + \zeta_{1,2} u_1 = -\frac{e}{m^*} (\vec{E}_0 \cdot \hat{u}_2) e^{i\vec{k} \cdot \vec{r}_2} \quad (\text{S2.2})$$

Substituting $\Omega_k = \sqrt{\omega_k^2 - \omega^2 - i\gamma_k \omega}$ for $k = 1, 2$ in equations (S2.1-S2.2) gives:

$$\Omega_1^2 u_1 + \zeta_{2,1} u_2 = -\frac{e}{m^*} (\vec{E}_0 \cdot \hat{u}_1) e^{i\vec{k} \cdot \delta \vec{r}_1} e^{i\vec{k} \cdot \vec{r}_0} \quad (\text{S3.1})$$

$$\Omega_2^2 u_2 + \zeta_{1,2} u_1 = -\frac{e}{m^*} (\vec{E}_0 \cdot \hat{u}_2) e^{i\vec{k} \cdot \delta \vec{r}_2} e^{i\vec{k} \cdot \vec{r}_0} \quad (\text{S3.2})$$

Solving equations (S3.1-S3.2) simultaneously results in the final expressions for $u_1(\omega)$ and $u_2(\omega)$ given by equations (2.1-2.2) in the manuscript.

Section S2. Current density response calculation

The current density response is calculated for a volume ΔV of the medium containing N_0 unit-cells (Supplementary Figure S1), each consisting of the two electron oscillators, by performing the following averaging operation detailed in (29):

$$\vec{j} = \frac{-e}{\Delta V} \sum_{\vec{r}_0 \in \Delta V} \left[\frac{\partial \vec{u}_1(\vec{r}_0, t)}{\partial t} \Big|_{\vec{r}_0 = \vec{r} - \delta \vec{r}_1} + \frac{\partial \vec{u}_2(\vec{r}_0, t)}{\partial t} \Big|_{\vec{r}_0 = \vec{r} - \delta \vec{r}_2} \right] \quad (\text{S4})$$

Evaluating this expression results in:

$$\vec{j} = -en \left[\frac{\partial \vec{u}_1(\vec{r}_0, t)}{\partial t} \Big|_{\vec{r}_0 = \vec{r} - \delta \vec{r}_1} + \frac{\partial \vec{u}_2(\vec{r}_0, t)}{\partial t} \Big|_{\vec{r}_0 = \vec{r} - \delta \vec{r}_2} \right] \quad (\text{S5})$$

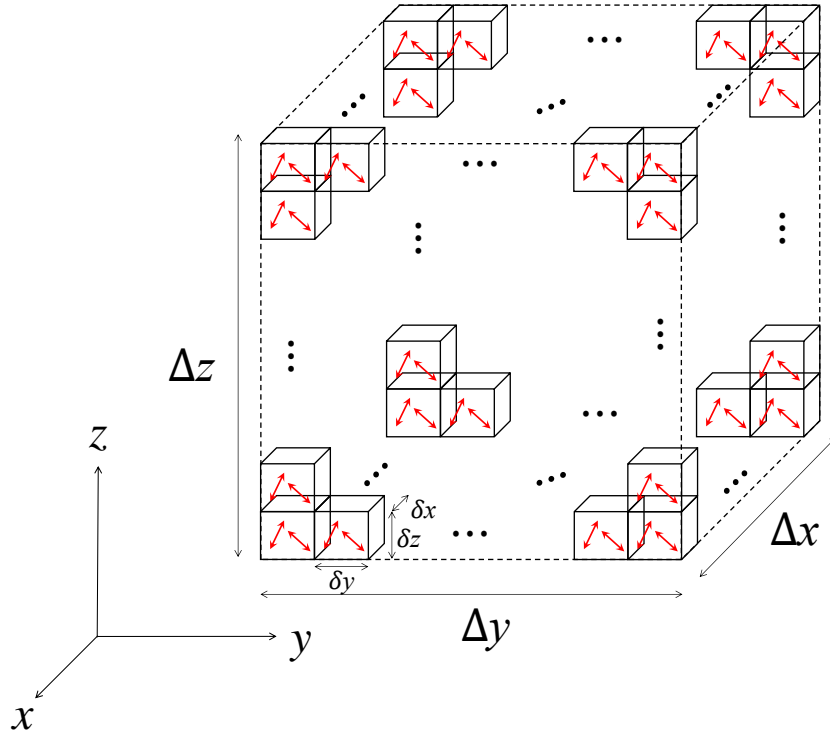


Fig. S1. Arrangement of bi-oscillator molecular unit-cells in a representative volume of optical media. A representative volume of media is defined as $\Delta V = \Delta x \Delta y \Delta z$ containing N_0 unit-cells, each consisting of the two oscillators. This is used in the calculation of the total current density response \vec{j} . Each unit-cell itself is assumed to occupy a volume $\delta V = \delta x \delta y \delta z$ assuming $\delta x, \delta y, \delta z \ll \lambda_0$ where λ_0 is the free-space wavelength.

Inserting equations (2.1-2.2) of the manuscript in equation (S5) along with the plasma frequency expressed as $\omega_p = \sqrt{ne^2/m^*\epsilon_0}$ where $n = N_0/\Delta V$ results in:

$$\vec{J} = \frac{-i\epsilon_0\omega\omega_p^2}{\Omega_1^2\Omega_2^2 - \zeta_{1,2}\zeta_{2,1}} \left\{ \left[\Omega_2^2(\vec{E}_0 \cdot \hat{u}_1) - \zeta_{2,1}(\vec{E}_0 \cdot \hat{u}_2)e^{-i\vec{k}\cdot(\delta\vec{r}_1 - \delta\vec{r}_2)} \right] \hat{u}_1 + \left[\Omega_1^2(\vec{E}_0 \cdot \hat{u}_2) - \zeta_{1,2}(\vec{E}_0 \cdot \hat{u}_1)e^{i\vec{k}\cdot(\delta\vec{r}_1 - \delta\vec{r}_2)} \right] \hat{u}_2 \right\} e^{i(\vec{k}\cdot\vec{r} - \omega t)} \quad (\text{S6})$$

Section S3. Homogeneous material parameters

The susceptibility terms are calculated by expressing equation (S6) in the form $\vec{J} = -i\omega\epsilon_0\chi\vec{E}_0 e^{i(\vec{k}\cdot\vec{r} - \omega t)}$, and extracting the tensor elements:

$$\chi_{xx} = \frac{\omega_p^2}{(\Omega_1^2\Omega_2^2 - \zeta_{1,2}\zeta_{2,1})} \left[(\Omega_1^2 \sin^2 \theta_2 \cos^2 \phi_2 + \Omega_2^2 \sin^2 \theta_1 \cos^2 \phi_1) - (\zeta_{1,2}e^{-i\vec{k}\cdot(\delta\vec{r}_1 - \delta\vec{r}_2)} + \zeta_{2,1}e^{i\vec{k}\cdot(\delta\vec{r}_1 - \delta\vec{r}_2)}) \sin \theta_1 \cos \phi_1 \sin \theta_2 \cos \phi_2 \right] \quad (\text{S7.1})$$

$$\chi_{xy} = \frac{\omega_p^2}{(\Omega_1^2\Omega_2^2 - \zeta_{1,2}\zeta_{2,1})} \left[(\Omega_1^2 \sin^2 \theta_2 \sin \phi_2 \cos \phi_2 + \Omega_2^2 \sin^2 \theta_1 \sin \phi_1 \cos \phi_1) - (\zeta_{1,2} \cos \phi_1 \sin \phi_2 e^{-i\vec{k}\cdot(\delta\vec{r}_1 - \delta\vec{r}_2)} + \zeta_{2,1} \sin \phi_1 \cos \phi_2 e^{i\vec{k}\cdot(\delta\vec{r}_1 - \delta\vec{r}_2)}) \sin \theta_1 \sin \theta_2 \right] \quad (\text{S7.2})$$

$$\chi_{xz} = \frac{\omega_p^2}{(\Omega_1^2\Omega_2^2 - \zeta_{1,2}\zeta_{2,1})} \left[(\Omega_1^2 \sin \theta_2 \cos \theta_2 \cos \phi_2 + \Omega_2^2 \sin \theta_1 \cos \theta_1 \cos \phi_1) - (\zeta_{1,2} \sin \theta_1 \cos \phi_1 \cos \theta_2 e^{-i\vec{k}\cdot(\delta\vec{r}_1 - \delta\vec{r}_2)} + \zeta_{2,1} \cos \theta_1 \sin \theta_2 \cos \phi_2 e^{i\vec{k}\cdot(\delta\vec{r}_1 - \delta\vec{r}_2)}) \right] \quad (\text{S7.3})$$

$$\chi_{yx} = \frac{\omega_p^2}{(\Omega_1^2\Omega_2^2 - \zeta_{1,2}\zeta_{2,1})} \left[(\Omega_1^2 \sin^2 \theta_2 \sin \phi_2 \cos \phi_2 + \Omega_2^2 \sin^2 \theta_1 \sin \phi_1 \cos \phi_1) - (\zeta_{1,2} \sin \phi_1 \cos \phi_2 e^{-i\vec{k}\cdot(\delta\vec{r}_1 - \delta\vec{r}_2)} + \zeta_{2,1} \cos \phi_1 \sin \phi_2 e^{i\vec{k}\cdot(\delta\vec{r}_1 - \delta\vec{r}_2)}) \sin \theta_1 \sin \theta_2 \right] \quad (\text{S7.4})$$

$$\chi_{yy} = \frac{\omega_p^2}{(\Omega_1^2\Omega_2^2 - \zeta_{1,2}\zeta_{2,1})} \left[(\Omega_1^2 \sin^2 \theta_2 \sin^2 \phi_2 + \Omega_2^2 \sin^2 \theta_1 \sin^2 \phi_1) - (\zeta_{1,2}e^{-i\vec{k}\cdot(\delta\vec{r}_1 - \delta\vec{r}_2)} + \zeta_{2,1}e^{i\vec{k}\cdot(\delta\vec{r}_1 - \delta\vec{r}_2)}) \sin \theta_1 \sin \phi_1 \sin \theta_2 \sin \phi_2 \right] \quad (\text{S7.5})$$

$$\chi_{yz} = \frac{\omega_p^2}{(\Omega_1^2\Omega_2^2 - \zeta_{1,2}\zeta_{2,1})} \left[(\Omega_1^2 \sin \theta_2 \cos \theta_2 \sin \phi_2 + \Omega_2^2 \sin \theta_1 \cos \theta_1 \sin \phi_1) - (\zeta_{1,2} \sin \theta_1 \sin \phi_1 \cos \theta_2 e^{-i\vec{k}\cdot(\delta\vec{r}_1 - \delta\vec{r}_2)} + \zeta_{2,1} \cos \theta_1 \sin \theta_2 \sin \phi_2 e^{i\vec{k}\cdot(\delta\vec{r}_1 - \delta\vec{r}_2)}) \right] \quad (\text{S7.6})$$

$$\chi_{zx} = \frac{\omega_p^2}{(\Omega_1^2 \Omega_2^2 - \zeta_{1,2} \zeta_{2,1})} [(\Omega_1^2 \sin \theta_2 \cos \theta_2 \cos \phi_2 + \Omega_2^2 \sin \theta_1 \cos \theta_1 \cos \phi_1) - (\zeta_{1,2} \cos \theta_1 \sin \theta_2 \cos \phi_2 e^{-i\vec{k} \cdot (\delta\vec{r}_1 - \delta\vec{r}_2)} + \zeta_{2,1} \sin \theta_1 \cos \phi_1 \cos \theta_2 e^{i\vec{k} \cdot (\delta\vec{r}_1 - \delta\vec{r}_2)})] \quad (S7.7)$$

$$\chi_{zy} = \frac{\omega_p^2}{(\Omega_1^2 \Omega_2^2 - \zeta_{1,2} \zeta_{2,1})} [(\Omega_1^2 \sin \theta_2 \cos \theta_2 \sin \phi_2 + \Omega_2^2 \sin \theta_1 \cos \theta_1 \sin \phi_1) - (\zeta_{1,2} \cos \theta_1 \sin \theta_2 \sin \phi_2 e^{-i\vec{k} \cdot (\delta\vec{r}_1 - \delta\vec{r}_2)} + \zeta_{2,1} \sin \theta_1 \sin \phi_1 \cos \theta_2 e^{i\vec{k} \cdot (\delta\vec{r}_1 - \delta\vec{r}_2)})] \quad (S7.8)$$

$$\chi_{zz} = \frac{\omega_p^2}{(\Omega_1^2 \Omega_2^2 - \zeta_{1,2} \zeta_{2,1})} [(\Omega_1^2 \cos^2 \theta_2 + \Omega_2^2 \cos^2 \theta_1) - (\zeta_{1,2} e^{-i\vec{k} \cdot (\delta\vec{r}_1 - \delta\vec{r}_2)} + \zeta_{2,1} e^{i\vec{k} \cdot (\delta\vec{r}_1 - \delta\vec{r}_2)}) \cos \theta_1 \cos \theta_2] \quad (S7.9)$$

To calculate the modified dielectric tensor $\epsilon(k, \omega)$ and the non-locality tensor $\Gamma(k, \omega)$, the polarization density $\vec{P} = \vec{J}/(-i\omega)$ is evaluated:

$$\vec{P}(\omega, \vec{r}) = \epsilon_0 \chi \vec{E}_0 e^{i(\vec{k} \cdot \vec{r} - \omega t)} \quad (S8)$$

The susceptibility tensor is expressed as the sum of modified dielectric and non-locality tensors as:

$$\chi(k, \omega) = \epsilon(k, \omega) + ik\Gamma(k, \omega) \quad (S9)$$

with the modified dielectric and non-locality tensors written in matrix form as:

$$\epsilon = \begin{pmatrix} \epsilon_{xx} & \epsilon_{xy} & \epsilon_{xz} \\ \epsilon_{yx} & \epsilon_{yy} & \epsilon_{yz} \\ \epsilon_{zx} & \epsilon_{zx} & \epsilon_{zz} \end{pmatrix} \quad (S10)$$

$$\Gamma = \begin{pmatrix} \Gamma_{xx} & \Gamma_{xy} & \Gamma_{xz} \\ \Gamma_{yx} & \Gamma_{yy} & \Gamma_{yz} \\ \Gamma_{zx} & \Gamma_{zy} & \Gamma_{zz} \end{pmatrix} \quad (S11)$$

Note that the dielectric tensor ϵ is calculated from the modified dielectric tensor as $\epsilon(k, \omega) = \epsilon(k, \omega) + I$

where I is the identity matrix. For plane waves, the equivalency $ik\Gamma \equiv \Gamma(\hat{k} \cdot \vec{\nabla})$ holds, allowing one to write

the polarization density as $\vec{P}(\vec{r}, \omega) = \epsilon_0 [\epsilon + \Gamma(\hat{k} \cdot \vec{\nabla})] \vec{E}_0 e^{i(\vec{k} \cdot \vec{r} - \omega t)}$. Note that this expression is equivalent

to the result presented in ref. 29, $\vec{P}(\vec{r}, \omega) = \epsilon_0 (\epsilon + \Gamma_n \nabla_n) \vec{E}_0 e^{i(\vec{k} \cdot \vec{r} - \omega t)}$ where $\Gamma_n = \Gamma \hat{k} \cdot \hat{a}_n$. Expanding

equations (S7.1-S7.9) using equation (S9) results in the following expressions for the modified dielectric

and non-locality tensor elements given respectively as:

$$\epsilon_{xx} = \frac{\omega_p^2}{(\Omega_1^2 \Omega_2^2 - \zeta_{1,2} \zeta_{2,1})} [(\Omega_1^2 \sin^2 \theta_2 \cos^2 \phi_2 + \Omega_2^2 \sin^2 \theta_1 \cos^2 \phi_1) - \cos[\vec{k} \cdot (\delta \vec{r}_1 - \delta \vec{r}_2)] (\zeta_{1,2} + \zeta_{2,1}) \sin \theta_1 \cos \phi_1 \sin \theta_2 \cos \phi_2] \quad (\text{S12.1})$$

$$\epsilon_{xy} = \frac{\omega_p^2}{(\Omega_1^2 \Omega_2^2 - \zeta_{1,2} \zeta_{2,1})} [(\Omega_1^2 \sin^2 \theta_2 \sin \phi_2 \cos \phi_2 + \Omega_2^2 \sin^2 \theta_1 \sin \phi_1 \cos \phi_1) - \cos[\vec{k} \cdot (\delta \vec{r}_1 - \delta \vec{r}_2)] (\zeta_{1,2} \cos \phi_1 \sin \phi_2 + \zeta_{2,1} \sin \phi_1 \cos \phi_2) \sin \theta_1 \sin \theta_2] \quad (\text{S12.2})$$

$$\epsilon_{xz} = \frac{\omega_p^2}{(\Omega_1^2 \Omega_2^2 - \zeta_{1,2} \zeta_{2,1})} [(\Omega_1^2 \sin \theta_2 \cos \theta_2 \cos \phi_2 + \Omega_2^2 \sin \theta_1 \cos \theta_1 \cos \phi_1) - \cos[\vec{k} \cdot (\delta \vec{r}_1 - \delta \vec{r}_2)] (\zeta_{1,2} \sin \theta_1 \cos \phi_1 \cos \theta_2 + \zeta_{2,1} \cos \theta_1 \sin \theta_2 \cos \phi_2)] \quad (\text{S12.3})$$

$$\epsilon_{yx} = \frac{\omega_p^2}{(\Omega_1^2 \Omega_2^2 - \zeta_{1,2} \zeta_{2,1})} [(\Omega_1^2 \sin^2 \theta_2 \sin \phi_2 \cos \phi_2 + \Omega_2^2 \sin^2 \theta_1 \sin \phi_1 \cos \phi_1) - \cos[\vec{k} \cdot (\delta \vec{r}_1 - \delta \vec{r}_2)] (\zeta_{1,2} \sin \phi_1 \cos \phi_2 + \zeta_{2,1} \cos \phi_1 \sin \phi_2) \sin \theta_1 \sin \theta_2] \quad (\text{S12.4})$$

$$\epsilon_{yy} = \frac{\omega_p^2}{(\Omega_1^2 \Omega_2^2 - \zeta_{1,2} \zeta_{2,1})} [(\Omega_1^2 \sin^2 \theta_2 \sin^2 \phi_2 + \Omega_2^2 \sin^2 \theta_1 \sin^2 \phi_1) - \cos[\vec{k} \cdot (\delta \vec{r}_1 - \delta \vec{r}_2)] (\zeta_{1,2} + \zeta_{2,1}) \sin \theta_1 \sin \phi_1 \sin \theta_2 \sin \phi_2] \quad (\text{S12.5})$$

$$\epsilon_{yz} = \frac{\omega_p^2}{(\Omega_1^2 \Omega_2^2 - \zeta_{1,2} \zeta_{2,1})} [(\Omega_1^2 \sin \theta_2 \cos \theta_2 \sin \phi_2 + \Omega_2^2 \sin \theta_1 \cos \theta_1 \sin \phi_1) - \cos[\vec{k} \cdot (\delta \vec{r}_1 - \delta \vec{r}_2)] (\zeta_{1,2} \sin \theta_1 \sin \phi_1 \cos \theta_2 + \zeta_{2,1} \cos \theta_1 \sin \theta_2 \sin \phi_2)] \quad (\text{S12.6})$$

$$\epsilon_{zx} = \frac{\omega_p^2}{(\Omega_1^2 \Omega_2^2 - \zeta_{1,2} \zeta_{2,1})} [(\Omega_1^2 \sin \theta_2 \cos \theta_2 \cos \phi_2 + \Omega_2^2 \sin \theta_1 \cos \theta_1 \cos \phi_1) - \cos[\vec{k} \cdot (\delta \vec{r}_1 - \delta \vec{r}_2)] (\zeta_{1,2} \cos \theta_1 \sin \theta_2 \cos \phi_2 + \zeta_{2,1} \sin \theta_1 \cos \phi_1 \cos \theta_2)] \quad (\text{S12.7})$$

$$\epsilon_{zy} = \frac{\omega_p^2}{(\Omega_1^2 \Omega_2^2 - \zeta_{1,2} \zeta_{2,1})} [(\Omega_1^2 \sin \theta_2 \cos \theta_2 \sin \phi_2 + \Omega_2^2 \sin \theta_1 \cos \theta_1 \sin \phi_1) - \cos[\vec{k} \cdot (\delta \vec{r}_1 - \delta \vec{r}_2)] (\zeta_{1,2} \cos \theta_1 \sin \theta_2 \sin \phi_2 + \zeta_{2,1} \sin \theta_1 \sin \phi_1 \cos \theta_2)] \quad (\text{S12.8})$$

$$\epsilon_{zz} = \frac{\omega_p^2}{(\Omega_1^2 \Omega_2^2 - \zeta_{1,2} \zeta_{2,1})} [(\Omega_1^2 \cos^2 \theta_2 + \Omega_2^2 \cos^2 \theta_1) - \cos[\vec{k} \cdot (\delta \vec{r}_1 - \delta \vec{r}_2)] (\zeta_{1,2} + \zeta_{2,1}) \cos \theta_1 \cos \theta_2] \quad (\text{S12.9})$$

and,

$$\Gamma_{xx} = \frac{\omega_p^2}{\Omega_1^2 \Omega_2^2 - \zeta_{1,2} \zeta_{2,1}} \left[\frac{\sin[\vec{k} \cdot (\delta \vec{r}_1 - \delta \vec{r}_2)]}{k} (\zeta_{1,2} - \zeta_{2,1}) \sin \theta_1 \cos \phi_1 \sin \theta_2 \cos \phi_2 \right] \quad (\text{S13.1})$$

$$\Gamma_{xy} = \frac{\omega_p^2}{(\Omega_1^2 \Omega_2^2 - \zeta_{1,2} \zeta_{2,1})} \left[\frac{\sin[\vec{k} \cdot (\delta \vec{r}_1 - \delta \vec{r}_2)]}{k} (\zeta_{1,2} \sin \phi_1 \cos \phi_2 - \zeta_{2,1} \sin \phi_2 \cos \phi_1) \sin \theta_1 \sin \theta_2 \right] \quad (\text{S13.2})$$

$$\Gamma_{xz} = \frac{\omega_p^2}{(\Omega_1^2 \Omega_2^2 - \zeta_{1,2} \zeta_{2,1})} \left[\frac{\sin[\vec{k} \cdot (\delta \vec{r}_1 - \delta \vec{r}_2)]}{k} (\zeta_{1,2} \cos \phi_2 \cos \theta_1 \sin \theta_2 - \zeta_{2,1} \cos \phi_1 \cos \theta_2 \sin \theta_1) \right] \quad (\text{S13.3})$$

$$\Gamma_{yx} = \frac{\omega_p^2}{(\Omega_1^2 \Omega_2^2 - \zeta_{1,2} \zeta_{2,1})} \left[\frac{\sin[\vec{k} \cdot (\delta \vec{r}_1 - \delta \vec{r}_2)]}{k} (\zeta_{1,2} \sin \phi_2 \cos \phi_1 - \zeta_{2,1} \sin \phi_1 \cos \phi_2) \sin \theta_1 \sin \theta_2 \right] \quad (\text{S13.4})$$

$$\Gamma_{yy} = \frac{\omega_p^2}{\Omega_1^2 \Omega_2^2 - \zeta_{1,2} \zeta_{2,1}} \left[\frac{\sin[\vec{k} \cdot (\delta \vec{r}_1 - \delta \vec{r}_2)]}{k} (\zeta_{1,2} - \zeta_{2,1}) \sin \theta_1 \sin \phi_1 \sin \theta_2 \sin \phi_2 \right] \quad (\text{S13.5})$$

$$\Gamma_{yz} = \frac{\omega_p^2}{(\Omega_1^2 \Omega_2^2 - \zeta_{1,2} \zeta_{2,1})} \left[\frac{\sin[\vec{k} \cdot (\delta \vec{r}_1 - \delta \vec{r}_2)]}{k} (\zeta_{1,2} \cos \theta_1 \sin \theta_2 \sin \phi_2 - \zeta_{2,1} \cos \theta_2 \sin \theta_1 \sin \phi_1) \right] \quad (\text{S13.6})$$

$$\Gamma_{zx} = \frac{\omega_p^2}{(\Omega_1^2 \Omega_2^2 - \zeta_{1,2} \zeta_{2,1})} \left[\frac{\sin[\vec{k} \cdot (\delta \vec{r}_1 - \delta \vec{r}_2)]}{k} (\zeta_{1,2} \sin \theta_1 \cos \theta_2 \cos \phi_1 - \zeta_{2,1} \sin \theta_2 \cos \theta_1 \cos \phi_2) \right] \quad (\text{S13.7})$$

$$\Gamma_{zy} = \frac{\omega_p^2}{(\Omega_1^2 \Omega_2^2 - \zeta_{1,2} \zeta_{2,1})} \left[\frac{\sin[\vec{k} \cdot (\delta \vec{r}_1 - \delta \vec{r}_2)]}{k} (\zeta_{1,2} \sin \theta_1 \cos \theta_2 \sin \phi_1 - \zeta_{2,1} \sin \theta_2 \cos \theta_1 \sin \phi_2) \right] \quad (\text{S13.8})$$

$$\Gamma_{zz} = \frac{\omega_p^2}{\Omega_1^2 \Omega_2^2 - \zeta_{1,2} \zeta_{2,1}} \left[\frac{\sin[\vec{k} \cdot (\delta \vec{r}_1 - \delta \vec{r}_2)]}{k} (\zeta_{1,2} - \zeta_{2,1}) \cos \theta_1 \cos \theta_2 \right] \quad (\text{S13.9})$$

Section S4. Chiroptical response calculation

The current density response $\vec{J} = -i\omega\epsilon_0\chi\vec{E}_0 e^{i(\vec{k}\cdot\vec{r}-\omega t)}$ can be expanded as:

$$J_x \propto \chi_{xx}E_{0,x} + \chi_{xy}E_{0,y} + \chi_{xz}E_{0,z} \quad (\text{S14.1})$$

$$J_y \propto \chi_{yx}E_{0,x} + \chi_{yy}E_{0,y} + \chi_{yz}E_{0,z} \quad (\text{S14.2})$$

$$J_z \propto \chi_{zx}E_{0,x} + \chi_{zy}E_{0,y} + \chi_{zz}E_{0,z} \quad (\text{S14.3})$$

Where, $E_{0,i}$ for $i = x, y, z$ corresponds to the magnitude of the three components of the electric field in cartesian coordinates. Taking the absolute value squared of equation (S14) gives

$$|\vec{J}|^2 = \epsilon_0^2\omega^2|\chi\vec{E}_0|^2 = |J_x|^2 + |J_y|^2 + |J_z|^2 \quad (\text{S15})$$

Expanding this expression in cartesian coordinates results in:

$$|J_x|^2 \propto |\chi_{xx}E_{0,x}|^2 + |\chi_{xy}E_{0,y}|^2 + |\chi_{xz}E_{0,z}|^2 + \chi_{xx}\chi_{xy}^*E_{0,x}E_{0,y}^* + \chi_{xx}^*\chi_{xy}E_{0,x}^*E_{0,y} + \chi_{xy}\chi_{xz}^*E_{0,y}E_{0,z}^* + \chi_{xy}^*\chi_{xz}E_{0,y}^*E_{0,z} + \chi_{xx}\chi_{xz}^*E_{0,x}E_{0,z}^* + \chi_{xx}^*\chi_{xz}E_{0,x}^*E_{0,z} \quad (\text{S16.1})$$

$$|J_y|^2 \propto |\chi_{yx}E_{0,x}|^2 + |\chi_{yy}E_{0,y}|^2 + |\chi_{yz}E_{0,z}|^2 + \chi_{yx}\chi_{yy}^*E_{0,x}E_{0,y}^* + \chi_{yx}^*\chi_{yy}E_{0,x}^*E_{0,y} + \chi_{yy}\chi_{yz}^*E_{0,y}E_{0,z}^* + \chi_{yy}^*\chi_{yz}E_{0,y}^*E_{0,z} + \chi_{yx}\chi_{yz}^*E_{0,x}E_{0,z}^* + \chi_{yx}^*\chi_{yz}E_{0,x}^*E_{0,z} \quad (\text{S16.2})$$

$$|J_z|^2 \propto |\chi_{zx}E_{0,x}|^2 + |\chi_{zy}E_{0,y}|^2 + |\chi_{zz}E_{0,z}|^2 + \chi_{zx}\chi_{zy}^*E_{0,x}E_{0,y}^* + \chi_{zx}^*\chi_{zy}E_{0,x}^*E_{0,y} + \chi_{zy}\chi_{zz}^*E_{0,y}E_{0,z}^* + \chi_{zy}^*\chi_{zz}E_{0,y}^*E_{0,z} + \chi_{zx}\chi_{zz}^*E_{0,x}E_{0,z}^* + \chi_{zx}^*\chi_{zz}E_{0,x}^*E_{0,z} \quad (\text{S16.3})$$

The chiroptical response of the system is defined as $\Delta A = |\vec{J}^{RCP}|^2 - |\vec{J}^{LCP}|^2$. Inserting equation (S15) into this expression gives $\Delta A = \epsilon_0^2\omega^2(|\chi\vec{E}_0|^2 - |\chi\vec{E}_0^*|^2)$. Finally, inserting equations (S16.1 – S16.3) in this

ΔA expression results in:

$$\Delta A = \Delta|J_x|^2 + \Delta|J_y|^2 + \Delta|J_z|^2 \propto \begin{aligned} & [(\chi_{xy}\chi_{xz}^* - \chi_{xy}^*\chi_{xz}) + (\chi_{yy}\chi_{yz}^* - \chi_{yy}^*\chi_{yz}) + (\chi_{zy}\chi_{zz}^* - \chi_{zy}^*\chi_{zz})](E_{0,y}E_{0,z}^* - E_{0,y}^*E_{0,z}) + \\ & [(\chi_{xx}\chi_{xz}^* - \chi_{xx}^*\chi_{xz}) + (\chi_{yx}\chi_{yz}^* - \chi_{yx}^*\chi_{yz}) + (\chi_{zx}\chi_{zz}^* - \chi_{zx}^*\chi_{zz})](E_{0,x}E_{0,z}^* - E_{0,x}^*E_{0,z}) + \\ & [(\chi_{xx}\chi_{xy}^* - \chi_{xx}^*\chi_{xy}) + (\chi_{yx}\chi_{yy}^* - \chi_{yx}^*\chi_{yy}) + (\chi_{zx}\chi_{zy}^* - \chi_{zx}^*\chi_{zy})](E_{0,x}E_{0,y}^* - E_{0,x}^*E_{0,y}) \end{aligned} \quad (\text{S17})$$

The nanocuboids in Figure 2A of the manuscript are aligned parallel to the x - y plane ($\theta_1 = \theta_2 = \pi/2$).

Using this in equations (S12.1-S12.9) and (S13.1-S13.9) shows that $\epsilon_{z,i} = \epsilon_{i,z} = \Gamma_{z,i} = \Gamma_{i,z} = 0$ for $i = x, y$, reducing equation (S17) to:

$$\begin{aligned}
\Delta A \propto & 2i|E_0|^2 \cos \theta_0 \{[(\epsilon_{xx}\epsilon_{xy}^* - \epsilon_{xx}^*\epsilon_{xy}) + (\epsilon_{yx}\epsilon_{yy}^* - \epsilon_{yx}^*\epsilon_{yy})] + \\
& k^2[(\Gamma_{xx}\Gamma_{xy}^* - \Gamma_{xx}^*\Gamma_{xy}) + (\Gamma_{yx}\Gamma_{yy}^* - \Gamma_{yx}^*\Gamma_{yy})] + \\
& ik[(\epsilon_{xy}\Gamma_{xx}^* + \epsilon_{xy}^*\Gamma_{xx}) + (\epsilon_{yy}\Gamma_{yx}^* + \epsilon_{yy}^*\Gamma_{yx})] - \\
& ik[(\epsilon_{xx}\Gamma_{xy}^* + \epsilon_{xx}^*\Gamma_{xy}) + (\epsilon_{yx}\Gamma_{yy}^* + \epsilon_{yx}^*\Gamma_{yy})]\}
\end{aligned} \tag{S18}$$

Note that since $\Gamma_{xx} = 0$ and $(\Gamma_{xx}\Gamma_{xy}^* - \Gamma_{xx}^*\Gamma_{xy}) = (\Gamma_{yx}\Gamma_{yy}^* - \Gamma_{yx}^*\Gamma_{yy}) = 0$, equation (S18) further simplifies to:

$$\begin{aligned}
\Delta A = & 2i\epsilon_0^2 \omega^2 |E_0|^2 \cos \theta_0 \{[(\epsilon_{xx}\epsilon_{xy}^* - \epsilon_{xx}^*\epsilon_{xy}) + (\epsilon_{yx}\epsilon_{yy}^* - \epsilon_{yx}^*\epsilon_{yy})] + \\
& ik[(\epsilon_{xy}\Gamma_{xx}^* + \epsilon_{xy}^*\Gamma_{xx}) + (\epsilon_{yy}\Gamma_{yx}^* + \epsilon_{yy}^*\Gamma_{yx}) - (\epsilon_{yx}\Gamma_{yy}^* + \epsilon_{yx}^*\Gamma_{yy})]\}
\end{aligned} \tag{S19}$$

This equation can be written as the sum of two chiroptical contributions, $\Delta A = \Delta A_{\epsilon,\epsilon} + \Delta A_{\Gamma,\epsilon}$, expressed individually as:

$$\Delta A_{\epsilon,\epsilon} = 2\epsilon_0^2 \omega^2 |E_0|^2 \cos \theta_0 \text{Im}\{\epsilon_{xx}^*\epsilon_{xy} + \epsilon_{yx}^*\epsilon_{yy}\} \tag{S20.1}$$

$$\Delta A_{\Gamma,\epsilon} = 2\epsilon_0^2 \omega^2 |E_0|^2 \cos \theta_0 \text{Re}\{k[(\epsilon_{xy}\Gamma_{xx}^* - \epsilon_{xx}\Gamma_{xy}^*) + (\epsilon_{yy}\Gamma_{yx}^* - \epsilon_{yx}\Gamma_{yy}^*)]\} \tag{S20.2}$$

Section S5. Dependence of the κ on the difference between oscillator frequencies

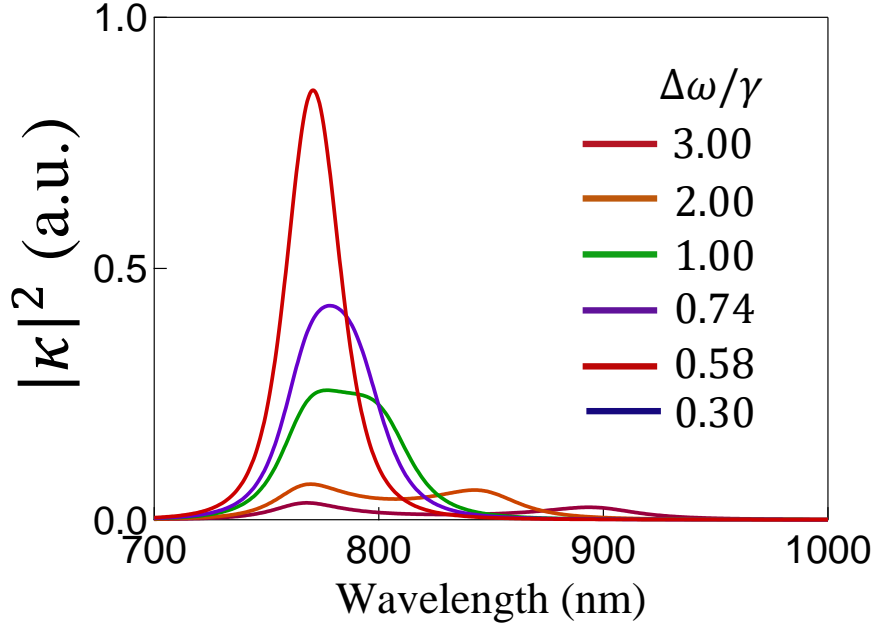


Fig. S2. Dependence of the multiplication factor κ on the difference between oscillator frequencies. The spectral plots for the dependence of $|\kappa|^2$ on $(\Delta\omega)/\gamma$ calculated under the conditions of Figure 3C in the manuscript. The magnitude of the multiplication factor decreases as the difference in oscillator frequencies $\Delta\omega$ becomes larger.

Section S6. Chiroptical response for two identical, orthogonally oriented nanocuboids at finite d_z

Schematic representation of two orthogonally oriented oscillators of identical lengths ($l_1 = l_2 = l$) corresponding to $\omega_1 = \omega_2 = \omega$, and symmetric cross-coupling strengths, $\zeta_{1,2}(\omega) = \zeta_{2,1}(\omega) = \zeta$, aligned orthogonal to each other ($\phi_1 = 90^\circ$ and $\phi_2 = 0^\circ$) and placed at $d_{1,y} = d_{2,x} = l/2$ separated by a distance d_z along the z -direction. Under these conditions, the modified dielectric tensor elements of equations (S12.1-S12.9) reduce to:

$$\epsilon_{xx} = \epsilon_{yy} = \Omega^2 \frac{\omega_p^2}{\Omega^4 - \zeta^2} \quad (\text{S21})$$

$\epsilon_{zz} = 0$ and $\epsilon_{i,j} = 0$ for $i \neq j$. The non-locality tensor elements given by equations (S13.1-S13.9) give $\Gamma_{i,j} = 0$ except for $i, j = x, y$. Assuming $kd_z \ll 1$, the remaining tensor elements are expressed as:

$$\Gamma_{xy} = -\Gamma_{yx} = \zeta d \frac{\omega_p^2}{\Omega^4 - \zeta^2} \quad (\text{S22})$$

The chiroptical response, calculated by inserting these tensor elements into equations (6.1) and (6.2) of the manuscript results in $\Delta A_{\epsilon,\epsilon} = 0$, and

$$\Delta A_{\Gamma,\epsilon} = 4\epsilon_0^2 \omega^2 \zeta d \omega_p^4 \frac{\Omega^2}{\zeta^2 - \Omega^4} \quad (\text{S23})$$

where the source field is assumed to have a unity magnitude, $|E_0|^2 = 1$. $\Delta A_{\Gamma,\epsilon}$ vs. λ_0 response results in a typical two-fold symmetric spectral lineshape characteristic of optical activity. Under identical conditions, the $\Delta A_{\Gamma,\epsilon}$ response is also calculated using equation (8.2) of the manuscript, demonstrating the equivalence of the two equations (6.2) and (8.2). The spectral lineshape is also consistent with the results of the Born-Kuhn model (20).

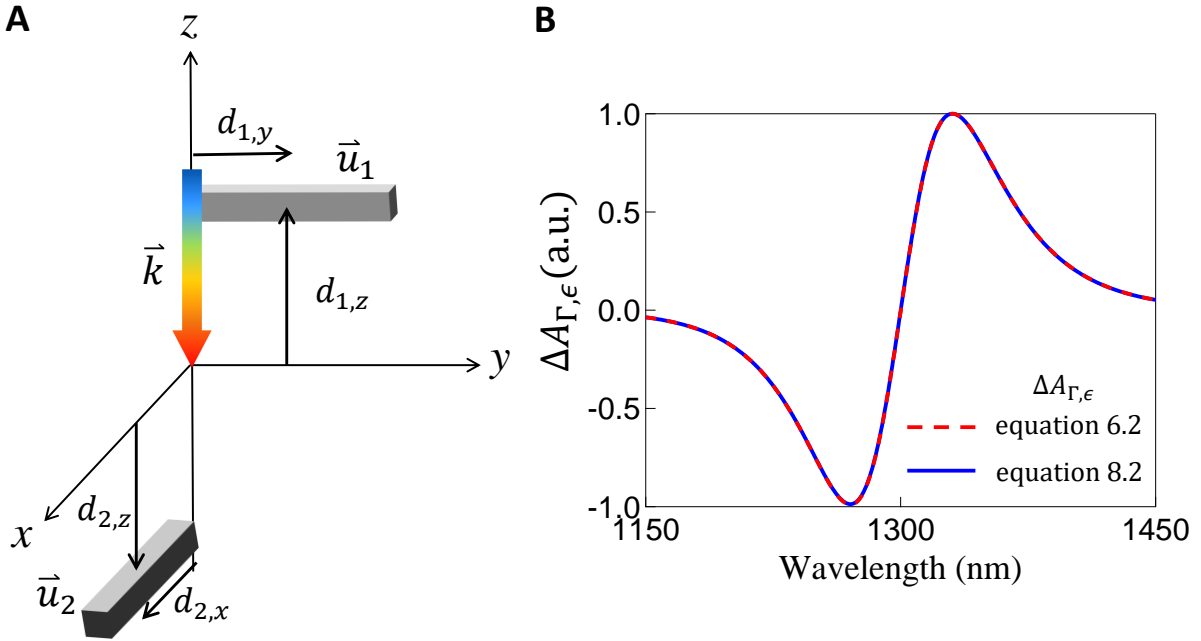


Fig. S3. Chiroptical response of orthogonally oriented identical nanocuboids in a three-dimensional arrangement. (A) Schematic representation of two orthogonally oriented Au nanocuboids, aligned parallel to the x - y plane ($\phi_1 = 90^\circ$ and $\phi_2 = 0^\circ$), excited by normally incident light ($\theta_0 = 0^\circ$). The two nanocuboids are located at $d_{1,z} = d_{2,z} = 50$ nm, and $d_{1,y} = d_{2,x} = 50$ nm, corresponding to $d_z = 100$ nm. The oscillators are designed to exhibit resonance at wavelengths of $\lambda_1 = \lambda_2 = 1300$ nm, and coupling strengths $\zeta_{1,2} = \zeta_{2,1} = 1 \times 10^{28} \text{ s}^{-1}$ as well as following values for the plasma frequency, $\omega_p = 1.37 \times 10^{16} \text{ s}^{-1}$, and damping coefficient, $\gamma = \gamma_1 = \gamma_2 = 1.22 \times 10^{14} \text{ s}^{-1}$, for Au in the near-infrared region are used in the calculations (32). (B) The calculated $\Delta A = \Delta A_{\Gamma,\epsilon}$ response obtained by simplifying equation (6.2) to

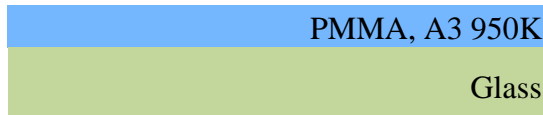
obtain equation (S23). For comparison, the $\Delta A_{r,\epsilon}$ response directly calculated using equation (8.2) is also shown, validating that they are equivalent.

Section S7. Device fabrication

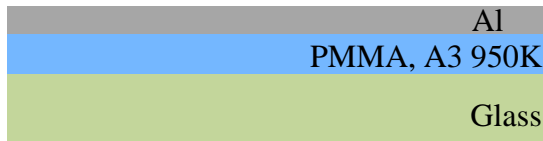
1. Clean glass substrate



2. Spin e-beam resist



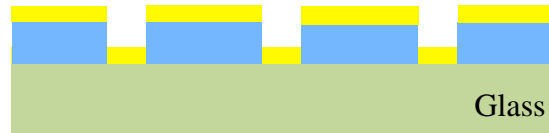
3. Thermal evaporation, Al 20 nm



4. E-beam lithography followed by Al etch and resist development



5. E-beam evaporation, Ti 2 nm, Au 40 nm



6. Lift-off in acetone bath



7. Representative SEM image

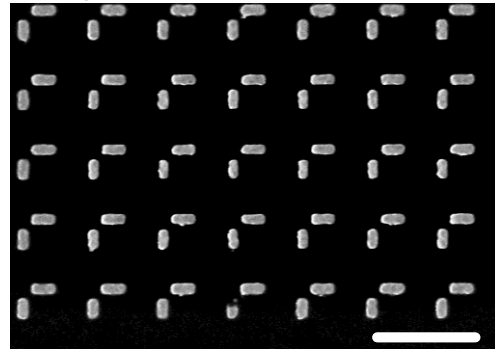


Fig. S4. Nanofabrication process steps. E-beam resist (PMMA) was spin-coated on a pre-cleaned fused silica substrate, followed by deposition of 20 nm Al film using thermal evaporation. E-beam lithography (at 100 keV) was used to expose the cuboid pattern on the resist, and the exposed resist was developed for 90 s in MIBK followed by 30 s rinse in IPA. Using E-beam evaporation, a 2 nm thick Ti adhesion layer, followed by 40 nm thick Au was deposited. Following deposition, lift-off was carried out by soaking the sample in acetone for twelve-hours. The lift-off procedure leaves Au islands at the location of the exposed regions. The scale bar in the representative top-down SEM image is 500 nm.

Section S8. Comparison between calculated CDA and ΔA spectral response

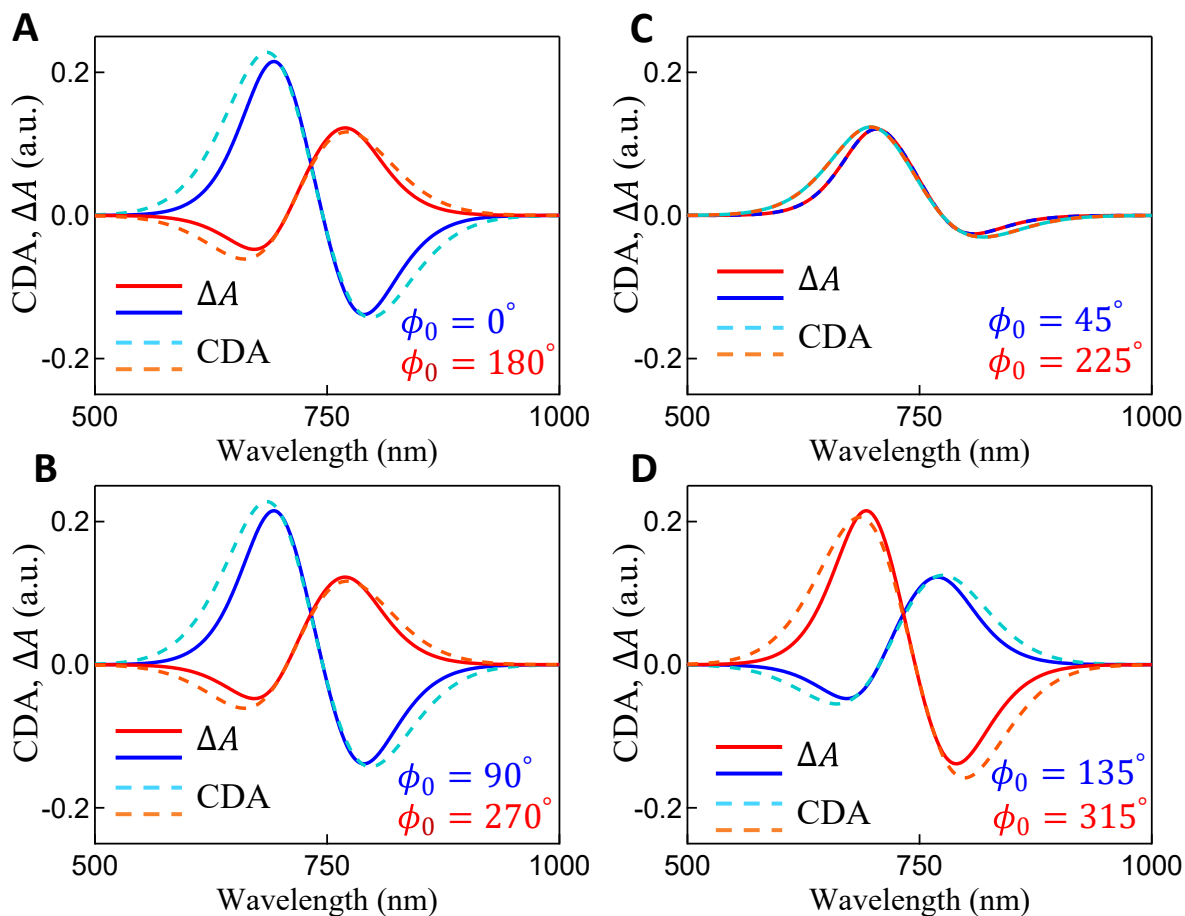


Fig. S5. Comparison between calculated CDA and ΔA spectral response. The calculated chiroptical responses CDA and ΔA calculated using the model for the exact structure and excitation conditions of Figure 5A of the manuscript. The similarity between the two response types, plotted at azimuthal angles: (A) $\phi_0 = 0^\circ$ (180°) (B) $\phi_0 = 45^\circ$ (225°) (C) $\phi_0 = 90^\circ$ (270°) and (D) $\phi_0 = 135^\circ$ (315°) verifies our assumption that they are equivalent measurements, and can be used interchangeably.

Section S9. Chiroptical response of 45° oriented cuboids of equal lengths

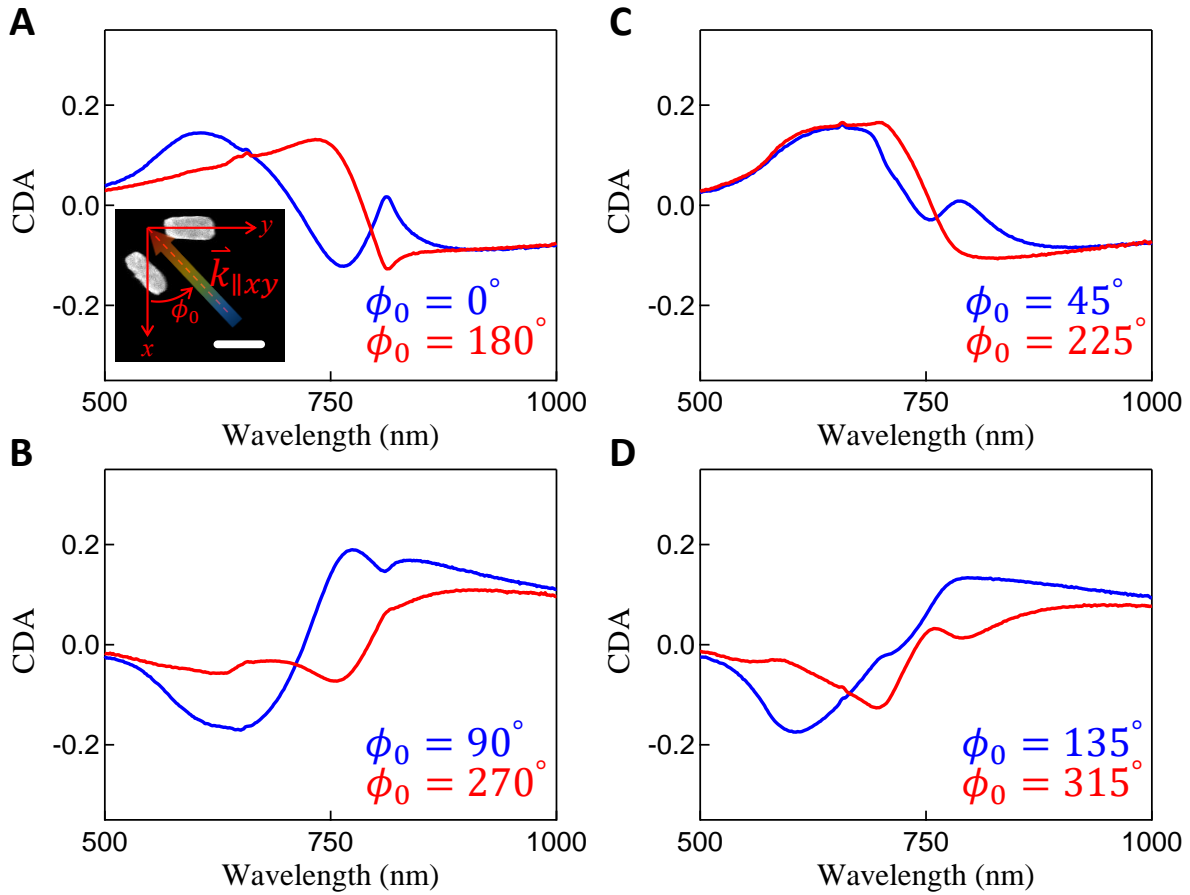


Fig. S6. Experimental measurements of the chiroptical response of 45° oriented cuboids of equal lengths. Experimental CDA measurements for an array of planar Au nanocuboid bi-oscillators, illuminated with free-space light between wavelengths of $\lambda_0 = 500$ nm and 1000 nm, as a function of incidence angle (varying ϕ_0 at a fixed $\theta_0 = 45^\circ$) for nanocuboids of equal lengths ($l_1 = l_2 = 120$ nm) oriented at 45° with respect to each other ($\phi_1 = 90^\circ$ and $\phi_2 = 45^\circ$). Top-down scanning-electron microscopy (SEM) images of unit-cells consisting of the two Au nanocuboid oscillators, overlaid with the coordinate system and orientation of the in-plane wavevector of the incident light ($\vec{k}_{\parallel xy}$) along the x - y plane, is shown as an inset in **A**. Scale bar represents 120 nm in the SEM image. (**A-D**) Experimentally measured CDA spectra at $\phi_0 = 0^\circ, 45^\circ, 90^\circ$ and 135° (blue plots), and at 180° offset from these angles (red plots) neither shows any clear symmetry in the spectral lineshape, nor a clear inversion in the sign for ϕ_0 rotation by 180° .

Section S10. Asymmetric transmission chiroptical response of all-dielectric media

For dielectric media, the electron-oscillators are bound and described here by amplitude oscillations \vec{u}_k of resonant frequencies $\omega_k = \sqrt{\alpha/m^*}$ for $k = 1, 2$ where α is a spring-constant, and m^* is the effective mass of a bound electron. The plasma frequency is replaced with $\widetilde{\omega}_b = \sqrt{\tilde{n}e^2/m^*\epsilon_0}$, where \tilde{n} is the density of bound electrons (39). The damping factor of the oscillators are assumed to be $\gamma_1 = \gamma_2 = \gamma$ and the cross-coupling amplitudes are assumed to be $\zeta_{1,2} = \zeta_{2,1} = 0$. Under these assumptions, all the non-locality tensor elements $\Gamma_{i,j}$ for $i, j = x, y, z$ become zero (equations (S13.1-S13.9)), and the modified dielectric tensor elements $\epsilon_{i,j}$ (equations (S12.1-S12.9)) are expressed as:

$$\epsilon_{xx} = \frac{\widetilde{\omega}_b^2}{\Omega_1^2 \Omega_2^2} (\Omega_1^2 \sin^2 \theta_2 \cos^2 \phi_2 + \Omega_2^2 \sin^2 \theta_1 \cos^2 \phi_1) \quad (\text{S24.1})$$

$$\epsilon_{xy} = \frac{\widetilde{\omega}_b^2}{\Omega_1^2 \Omega_2^2} (\Omega_1^2 \sin^2 \theta_2 \sin \phi_2 \cos \phi_2 + \Omega_2^2 \sin^2 \theta_1 \sin \phi_1 \cos \phi_1) \quad (\text{S24.2})$$

$$\epsilon_{xz} = \frac{\widetilde{\omega}_b^2}{\Omega_1^2 \Omega_2^2} (\Omega_1^2 \sin \theta_2 \cos \theta_2 \cos \phi_2 + \Omega_2^2 \sin \theta_1 \cos \theta_1 \cos \phi_1) \quad (\text{S24.3})$$

$$\epsilon_{yx} = \frac{\widetilde{\omega}_b^2}{\Omega_1^2 \Omega_2^2} (\Omega_1^2 \sin^2 \theta_2 \sin \phi_2 \cos \phi_2 + \Omega_2^2 \sin^2 \theta_1 \sin \phi_1 \cos \phi_1) \quad (\text{S24.4})$$

$$\epsilon_{yy} = \frac{\widetilde{\omega}_b^2}{\Omega_1^2 \Omega_2^2} (\Omega_1^2 \sin^2 \theta_2 \sin^2 \phi_2 + \Omega_2^2 \sin^2 \theta_1 \sin^2 \phi_1) \quad (\text{S24.5})$$

$$\epsilon_{yz} = \frac{\widetilde{\omega}_b^2}{\Omega_1^2 \Omega_2^2} (\Omega_1^2 \sin \theta_2 \cos \theta_2 \sin \phi_2 + \Omega_2^2 \sin \theta_1 \cos \theta_1 \sin \phi_1) \quad (\text{S24.6})$$

$$\epsilon_{yx} = \frac{\widetilde{\omega}_b^2}{\Omega_1^2 \Omega_2^2} (\Omega_1^2 \sin \theta_2 \cos \theta_2 \cos \phi_2 + \Omega_2^2 \sin \theta_1 \cos \theta_1 \cos \phi_1) \quad (\text{S24.7})$$

$$\epsilon_{yy} = \frac{\widetilde{\omega}_b^2}{\Omega_1^2 \Omega_2^2} (\Omega_1^2 \sin \theta_2 \cos \theta_2 \sin \phi_2 + \Omega_2^2 \sin \theta_1 \cos \theta_1 \sin \phi_1) \quad (\text{S24.8})$$

$$\epsilon_{yz} = \frac{\widetilde{\omega}_b^2}{\Omega_1^2 \Omega_2^2} (\Omega_1^2 \cos^2 \theta_2 + \Omega_2^2 \cos^2 \theta_1) \quad (\text{S24.9})$$

We define an impermeittivity tensor, $\boldsymbol{\rho}(k, \omega)$, in terms of the modified dielectric tensor, $\boldsymbol{\epsilon}(k, \omega)$, expressed as (36):

$$\boldsymbol{\rho}(k, \omega) = \boldsymbol{\epsilon}^{-1}(k, \omega) \quad (\text{S25})$$

with tensor elements $\rho_{i,j}$ for $i, j = 1, 2$ and 3.

The electric-flux density within the medium can be written as $\vec{D} = \hat{a}_1 D_1 + \hat{a}_2 D_2 + \hat{a}_3 D_3$ where $\hat{a}_1 = -\hat{a}_\phi$, $\hat{a}_2 = \hat{a}_\theta$, $\hat{a}_3 = \hat{a}_r$. The dispersion relation of the system is calculated using the relationship between electric flux density \vec{D} and electric field \vec{E} , given by $\vec{E} = \boldsymbol{\rho}\vec{D}$, and the relationship between magnetic field \vec{H} and magnetic flux density \vec{B} , given by $\vec{H} = \mu_0^{-1}\vec{B}$, where μ_0 is the permeability of free-space. From equation (S25) and the field expressions, results in the dispersion relation for an arbitrarily oriented source field expressed as (40):

$$\begin{pmatrix} u^2 - \mu_0^{-1}\rho_{11} & -\mu_0^{-1}\rho_{12} \\ -\mu_0^{-1}\rho_{21} & u^2 - \mu_0^{-1}\rho_{22} \end{pmatrix} \begin{pmatrix} D_1 \\ D_2 \end{pmatrix} = 0 \quad (\text{S26})$$

The phase velocities u_\pm for the eigenmodes of the system are found by setting the determinant of the matrix expression of equation (S26) equal to zero, resulting in:

$$u_\pm = Re \left\{ \sqrt{\frac{1}{2\mu_0} \left[(\rho_{11} + \rho_{22}) \pm \sqrt{(\rho_{11} - \rho_{22})^2 + 4\rho_{12}\rho_{21}} \right]} \right\} \quad (\text{S27})$$

The corresponding k -vectors for the eigenmodes, corresponding to the characteristic waves in the medium, are calculated using $k_\pm = \omega/u_\pm$ with the field components satisfying the relation:

$$\frac{D_2}{D_1} = \frac{2\rho_{21}}{(\rho_{11} - \rho_{22}) \pm \sqrt{(\rho_{11} - \rho_{22})^2 + 4\rho_{12}\rho_{21}}} \quad (\text{S28})$$

By choosing certain oscillator parameters, the characteristic waves satisfying equation (S28) can be made circularly polarized ($D_2/D_1 \approx \pm i$). One such set of parameters that satisfy this condition is achieved by setting the oscillator resonance wavelengths to $\lambda_1 = \lambda_2 = 450$ nm, and assuming the damping factor to be

$\gamma = 9.29 \times 10^{14} \text{ s}^{-1}$, and $\tilde{\omega}_b = 4.54 \times 10^{15} \text{ s}^{-1}$. Additionally, the first oscillator is assumed to be oriented at $\theta_1 = 165^\circ$ and $\phi_1 = 308^\circ$, and the second oscillator at $\theta_2 = 22^\circ$ and $\phi_2 = 156^\circ$. Inserting these assumptions in equation (S28), results in $D_2/D_1 \approx \pm i$ for a source field at normal incidence, $\theta_0 = 0^\circ$ (Supplementary Figure S7). The direction of power propagation for each eigenmode is determined from the direction normal to the k -surface, calculated from equations (S27) (40). As shown in Supplementary Figure S7D, the Poynting vectors \vec{S}_+ and \vec{S}_- , corresponding to the RCP and LCP components in this configuration, respectively, propagate in different directions. An additional deployment of geometric phase further enables independent phase-front manipulation of these two components (Fig. S7E). This illustrates that a strong far-field CO response may be measured in all-dielectric optical media through spatial filtering of either the RCP or the LCP light.

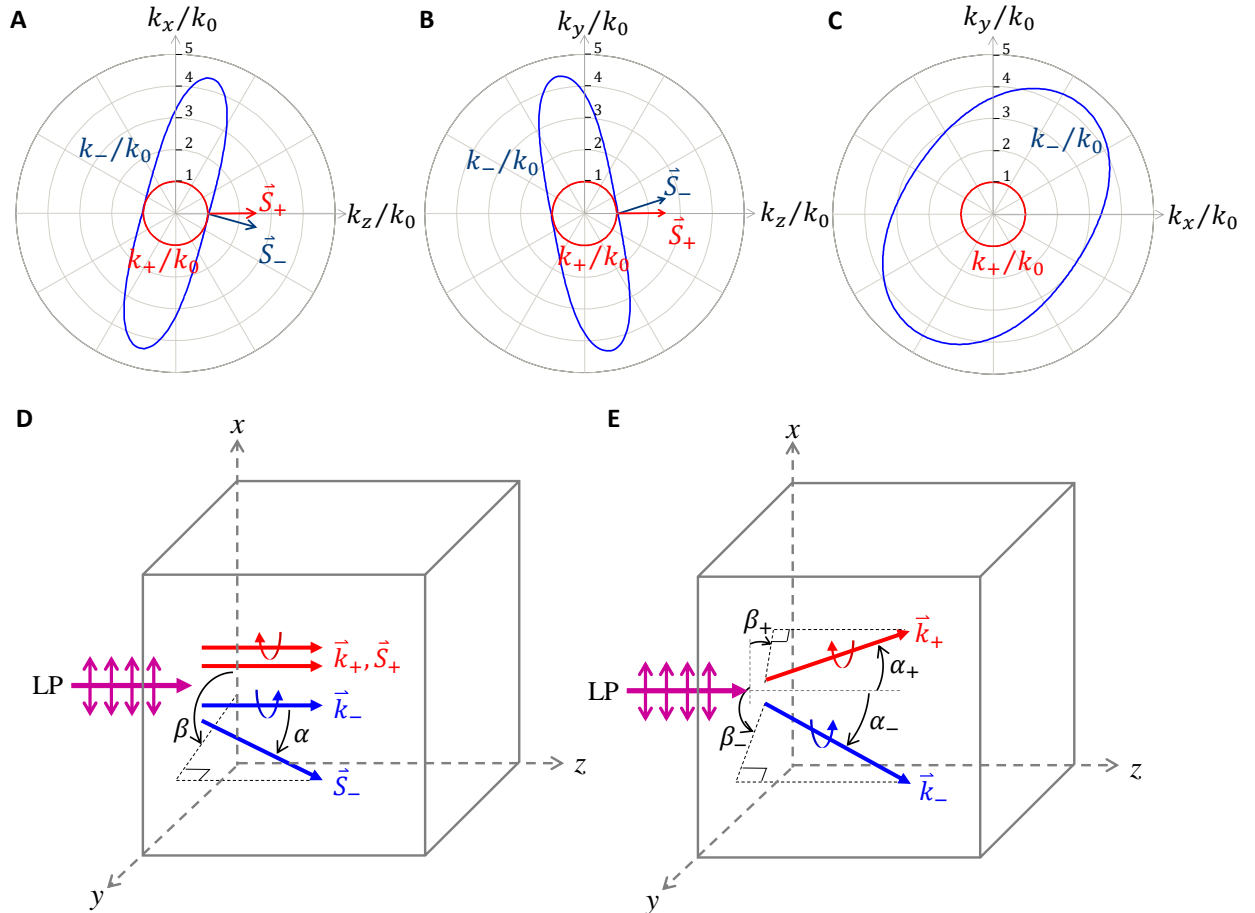


Fig. S7. Isofrequency surfaces and Poynting vectors for the eigenmodes of a biaxial medium. (A-C) The isofrequency surface plots in normalized k -space along the three characteristic planes corresponding to the right and left-handed eigenmodes, $k_+ = \omega/u_+$ (red) and $k_- = \omega/u_-$ (blue) respectively, of an all-dielectric biaxial medium. The eigenmodes are calculated at $\omega = 4.19 \times 10^{15} \text{ s}^{-1}$. The corresponding Poynting vectors (\vec{S}_+ and \vec{S}_- , for the RCP and LCP components, respectively) for a linearly polarized (LP) light normally incident on the medium, $\theta_0 = 0^\circ$, and propagating parallel to the z -direction is also shown. (D) A schematic of power propagation, in the medium, along different directions for the two characteristic opposite handedness waves. Although \vec{k}_+ and \vec{k}_- both propagate along the z -axis, the Poynting vectors for the two eigenmodes are not parallel. \vec{S}_+ continues to propagate along the z -axis, but \vec{S}_- propagates at an angle β relative to the x -axis and angle α relative to the z -axis. (E) The introduction of a geometric phase enables circular birefringence, where \vec{k}_+ and \vec{k}_- each refract at different angles α_+ (β_+) and α_- (β_-) relative to the z -axis (x -axis), respectively. This ability to manipulate wavefronts through geometric phase enable applications such as CP sensitive holographic imaging (24) and selective focusing of CP light (38).